Role of iodine oxoacids in atmospheric aerosol nucleation. 371, 589–595 (2021). doi: 10.1126/science.abe0298

Role of iodine oxoacids in atmospheric aerosol nucleation

Authors

Xu-Cheng He[1,*], Yee Jun Tham[1], Lubna Dada[1], Mingyi Wang[2], Henning Finkenzeller[3], Dominik Stolzenburg[4,1], Siddharth Iyer[5], Mario Simon[6], Andreas Kürten[6], Jiali Shen[1], Birte Rörup[1], Matti Rissanen[5], Siegfried Schobesberger[7], Rima Baalbaki[1], Dongyu S. Wang[8], Theodore K. Koenig[3], Tuija Jokinen[1], Nina Sarnela[1], Lisa J. Beck[1], João Almeida[9], Stavros Amanatidis[10], António Amorim[11], Farnoush Ataei[12], Andrea Baccarini[8], Barbara Bertozzi[13], Federico Bianchi[1], Sophia Brilke[4], Lucía Caudillo[6], Dexian Chen[2], Randall Chiu[3], Biwu Chu[1], António Dias[11], Aijun Ding[14], Josef Dommen[8], Jonathan Duplissy[1,15], Imad El Haddad[8], Loïc Gonzalez Carracedo[4], Manuel Granzin[6], Armin Hansel[16], Martin Heinritzi[6], Victoria Hofbauer[2], Heikki Junninen[17,1], Juha Kangasluoma[1], Deniz Kemppainen[1], Changhyuk Kim[10,18], Weimeng Kong[10], Jordan E. Krechmer[19], Aleksandr Kvashnin[20], Totti Laitinen[1], Houssni Lamkaddam[8], Chuan Ping Lee[8], Katrianne Lehtipalo[1,21], Markus Leiminger[16], Zijun Li[7], Vladimir Makhmutov[20], Hanna E. Manninen[9], Guillaume Marie[6], Ruby Marten[8], Serge Mathot[9], Roy L. Mauldin[22], Bernhard Mentler[16], Ottmar Möhler[13], Tatjana Müller[6], Wei Nie[14], Antti Onnela[9], Tuukka Petäjä[1], Joschka Pfeifer[9], Maxim Philippov[20], Ananth Ranjithkumar[23], Alfonso Saiz-López[24], Imre Salma[25], Wiebke Scholz[16,26], Simone Schuchmann[27], Benjamin Schulze[10], Gerhard Steiner[16], Yuri Stozhkov[20], Christian Tauber[4], António Tomé[28], Roseline C. Thakur[1], Olli Väisänen[7], Miguel Vazquez-Pufleau[4], Andrea C. Wagner[3,6], Yonghong Wang[1], Stefan K. Weber[9], Paul M. Winkler[4], Yusheng Wu[1], Mao Xiao[8], Chao Yan[1], Qing Ye[2], Arttu Ylisirniö[7], Marcel Zauner-Wieczorek[6], Qiaozhi Zha[1], Putian Zhou[1], Richard C. Flagan[10], Joachim Curtius[6], Urs Baltensperger[8], Markku Kulmala[1,14,15,29], Veli-Matti Kerminen[1], Theo Kurtén[30], Neil M. Donahue[2,31,32,33], Rainer Volkamer[3], Jasper Kirkby[9,6 *], Douglas R. Worsnop[19,1], Mikko Sipilä[1,*]

Affiliations

[1]Institute for Atmospheric and Earth System Research / Physics, Faculty of Science, P. O. Box 64, 00014 University of Helsinki, Helsinki, Finland
[2]Center for Atmospheric Particle Studies, Carnegie Mellon University, Pittsburgh, PA, 15213, USA
[3]Department of Chemistry & CIRES, UCB215, University of Colorado Boulder, Boulder, CO 80309, USA
[4]Faculty of Physics, University of Vienna, Boltzmanngasse 5, 1090 Vienna, Austria
[5]Aerosol Physics Laboratory, Physics Unit, Faculty of Engineering and Natural Sciences, Tampere University, Tampere, Finland
[6]Institute for Atmospheric and Environmental Sciences, Goethe University Frankfurt, Frankfurt am Main, 60438, Germany
[7]Department of Applied Physics, PL 1627, University of Eastern Finland, 70211 Kuopio, Finland
[8]Laboratory of Atmospheric Chemistry, Paul Scherrer Institute, CH-5232 Villigen, Switzerland
[9]CERN, the European Organization for Nuclear Research, CH-1211 Geneve 23, Switzerland
[10]Division of Chemistry and Chemical Engineering, California Institute of Technology, Pasadena, CA 91125, USA
[11]CENTRA and Faculdade de Ciências da Universidade de Lisboa, Campo Grande, 1749-016 Lisboa, Portugal
[12]Leibnbiz Institute fot Tropospheric Research, 04318 Leipzig, Germany
[13]Institute of Meteorology and Climate Research, Karlsruhe Institute of Technology, Hermann-von-Helmholtz-Platz 1, D-76344 Eggenstein-Leopoldshafen, Germany
[14]Joint International Research Laboratory of Atmosopheric and Earth System Sciences, School of Atmospheric Sciences, Nanjing University
[15]Helsinki Institute of Physics, P.O. Box 64 (Gustaf Hallstromin katu 2), FI-00014 University of Helsinki, Finland
[16]Institute of Ion Physics and Applied Physics, University of Innsbruck, Technikerstraße 25, 6020 Innsbruck, Austria
[17]Institute of Physics, University of Tartu, Otwaldi 1, 50411, Tartu, Estonia
[18]School of Civil and Environmental Engineering, Pusan National University, Busan 46241, Republic of Korea
[19]Aerodyne Research, Inc., 45 Manning Dr., Billerica, MA 01821-3934
[20]P.N. Lebedev Physical Institute of the Russian Academy of Sciences, 53 Leninskiy Prospekt, 119991, Moscow, Russia
[21]Finnish meteorological institute, Erik Palmenin aukio 1, 00560 Helsinki, Finland
[22]Department of Atmospheric and Oceanic Sciences, University of Colorado, Boulder, CO 80309 USA
[23]School of Earth and Environment, University of Leeds, Leeds, LS2 9JT, UK
[24]Department of Atmospheric Chemistry and Climate, Instituto de Química Física Rocasolano, CSIC, Spain
[25]Institute of Chemistry, Eötvös University, Pázmány stny. 1/A, H-1117 Budapest, Hungary
[26]Ionicon Analytik Ges.m.b.H., Eduard-Bodem-Gasse 3, 6020 Innsbruck, Austria
[27]Johannes Gutenberg-University Mainz, 55099 Mainz, Germany
[28]Institute Infante Dom Luíz, University of Beira Interior, Rua Marquês D'Ávila e Bolama 6201-001 Covilhã, Portugal
[29]Aerosol and Haze Laboratory, Beijing Advanced Innovation Center for Soft Matter Science and Engineering, Beijing University of Chemical Technology, Beijing, China
[30]Department of Chemistry, University of Helsinki, P.O. Box 55, 00014 University of Helsinki, Helsinki, Finland

[31]Department of Chemistry, Carnegie Mellon University, Pittsburgh, PA, 15213, USA
[32]Department of Chemical Engineering, Carnegie Mellon University, Pittsburgh, PA, 15213, USA
[33]Department of Engineering and Public Policy, Carnegie Mellon University, Pittsburgh, PA, 15213, USA

*Corresponding authors. Email: xucheng.he@helsinki.fi (X.-C.H.), jasper.kirkby@cern.ch (J.Ki) and mikko.sipila@helsinki.fi (M.Sip.)

Abstract:

Iodic acid (HIO_3) is known to form aerosol particles in coastal marine regions; but predicted nucleation and growth rates are lacking. Here, using the CERN CLOUD chamber, we find the nucleation rates of HIO_3 particles are rapid, even exceeding sulfuric acid-ammonia rates under similar conditions. We find ion-induced nucleation involves IO_3^- and the sequential addition of HIO_3, and it proceeds at the kinetic limit below +10 °C. In contrast, neutral nucleation involves the repeated sequential addition of iodous acid (HIO_2) then HIO_3, showing that HIO_2 plays a key stabilizing role. Freshly formed particles are composed almost entirely of HIO_3, which drives rapid particle growth at the kinetic limit. Our measurements indicate that iodine oxoacid particle formation can compete with sulfuric acid in pristine regions of the atmosphere.

One Sentence Summary

Iodic acid (HIO_3) and iodous acid (HIO_2) rapidly form new particles and can compete with sulfuric acid in pristine regions.

New particle formation plays an important role in radiative forcing of the climate. If particles survive to larger sizes, they influence climate directly by scattering light and indirectly by producing more than half of all cloud condensation nuclei (CCN) (*1*). However, new particle formation and aerosol-cloud interactions remain relatively poorly understood and constitute major uncertainties in determining Earth's equilibrium climate sensitivity with climate models (*2*). So far, only a few vapors that can form new particles under atmospheric conditions have been identified. They comprise sulfuric acid (*3*–*7*), methanesulfonic acid (*3*, *8*), iodine species (*9*–*11*), highly oxygenated organic molecules (HOMs) (*12*) and, more recently, nitric acid (*13*). Under warm conditions or low vapor concentrations, acidic molecular clusters further require base vapors such as ammonia (*6*, *13*, *14*) or dimethylamine (*15*) to stabilize them against evaporation. Ions can play a comparable role in stabilizing nucleating acidic (*6*) or biogenic (*12*) particles.

Marine new particle formation is especially important as the ocean is vast, and marine clouds are highly sensitive to CCN since their number concentrations are low. Marine clouds are radiatively important since they have a high infrared emission and albedo in contrast with the dark ocean surface. Marine new particle formation has thus been a focus for aerosol-climate interactions and feedbacks for many years (*16*), mostly concerning dimethylsulfide and its oxidation products (*3*, *8*, *16*). Although nucleation of iodine oxides was first studied almost twenty years ago (*9*, *10*), iodine particle formation is presently considered to have limited global significance (*17*) and remains relatively poorly understood.

The ocean surface is a major source of atmospheric iodine; hypoiodous acid (HOI) and molecular iodine (I_2) are emitted by the reaction of gaseous ozone with aqueous iodide (I^-) (*18*). Typical daytime emissions from the tropical Atlantic Ocean are 7×10^7 HOI molecules $cm^{-2}\ s^{-1}$ and 7×10^6 I_2 molecules $cm^{-2}\ s^{-1}$ (*18*), leading to daytime mixing ratios in the marine boundary layer of around 1 pptv HOI and 0.1 pptv iodine atoms (*19*). Land surfaces (vegetation and soils) emit comparable iodine fluxes as iodomethane (CH_3I), producing boundary layer mixing ratios around 0.5 pptv and free tropospheric levels around 0.1 pptv (*20*). Iodine compounds have been found at widespread sites that include coastal regions (*9*, *10*), Arctic sea ice (*11*, *21*), the marine boundary layer (*22*), the lower (*23*) and upper free troposphere (*24*), and the stratosphere (*25*).

More recently, iodic acid (HIO_3) has been shown to drive coastal marine new particle formation at Mace Head, Ireland (*11*), and intense iodine particle formation has been reported along China's coast (*26*). So far, however, controlled laboratory experiments under atmospheric conditions are lacking and so atmospheric observations of HIO_3 cannot be connected with predicted particle formation and growth rates. A mechanism for HIO_3 nucleation has been identified (*11*) but the ion-induced (charged) and neutral (uncharged) clusters were unseparated, and may involve different iodine compounds. Furthermore, iodine oxides (I_xO_y) are presently considered to be the major species responsible for the growth and composition of iodic particles (*9*, *10*, *27*) although, once again, experimental measurements under atmospheric conditions are lacking.

Nucleation and growth rates

Here we report iodine new particle formation experiments performed under marine boundary layer conditions in the CERN CLOUD chamber (Cosmics Leaving OUtdoor Droplets; see Methods) between September 2017 and November 2019. The experiments were conducted at +10 °C and

-10 °C, at 34-73 % relative humidity (RH) and 20-46 ppbv ozone. We introduced molecular iodine from an evaporator (0.4-168 pptv, median I_2 = 6.4 pptv) in the chamber.

The formation pathways of iodine oxoacids from iodine precursor vapors are not well understood, although computational studies assume that HO_x radicals are required to produce HIO_3 (*28*, *29*). We tested this hypothesis by using green light (528 nm) alone to photolyze I_2 into iodine atoms. At full intensity, CLOUD's green light source photolyzes iodine vapor at a rate of 7×10^{-3} s^{-1}, although most experiments were carried out at relative intensities of 10–20 %. Green light does not produce significant amount of HO_x since it cannot photolyze O_3. Nevertheless, we found that iodine atoms are rapidly oxidized in the presence of water vapor and ozone to produce both HIO_3 and iodous acid (HIO_2; Fig. S1). Iodine oxoacids can form from hydrated iodine atoms and iodine oxide radicals reacting with ozone, and from hydrolysis of I_xO_y (*27*). Under our experimental conditions, photolysis of I_2 typically produces 2×10^5 I atom cm^{-3} s^{-1}, and roughly ~1 pptv iodine monoxide (IO) radicals. The full range of conditions probed includes IO concentrations found in the open ocean marine boundary layer and remote free troposphere (*18, 19, 23, 24*; Table S1). Notably, at constant actinic flux, HIO_3 acid increases linearly with iodine concentration, whereas HIO_2 increases as the square root (Fig. S2). We speculate that iodine oxoacids form at CLOUD either from iodine radicals, *e.g.* $I + H_2O + O_3 \rightarrow HIO_3 + OH$, or the initial I_xO_y intermediates (*e.g.* $I_2O_2 + H_2O \rightarrow HIO_2 + HOI$). Since ozone and water vapor are found throughout the troposphere, our findings imply that molecular iodine will produce iodine oxoacids even under cloudy daylight conditions with negligible ultraviolet irradiation.

We show in Fig. 1A our measured nucleation rates at 1.7 nm, $J_{1.7}$, versus the HIO_3 concentration at +10 °C and -10 °C, and under three ionization conditions: neutral, J_n (ions eliminated from the chamber by a 20 kV m^{-1} electric field); galactic cosmic ray, J_{gcr} (boundary layer ion pair concentrations of around 700 cm^{-3}) and beam enhanced, J_{beam} (ion pair concentrations around 2500 cm^{-3}, comparable to the upper free troposphere). The measurements were performed at contaminant ammonia levels near 3 pptv. The nucleation rates show a strong dependency on HIO_3 concentration, charge and temperature. There is a large ion enhancement of the nucleation rate at +10 °C, whereas J_{gcr} and J_n are comparable at -10 °C. The nucleation rate increases rapidly as the temperature falls from +10 °C to -10 °C. For comparison, we include in Fig. 1A our previous measurements of J_{gcr} at 1.7 nm for sulfuric acid with 100 pptv NH_3 (*14*), which show that the nucleation rate of iodine oxoacids exceeds that of $H_2SO_4 - NH_3$ at the same acid concentrations.

In Fig. 1B we show the dependence on HIO_3 concentration of the particle growth rates between 1.8 and 3.2 nm, at +10 °C and -10 °C. The growth rates of iodine oxoacid particles at +10 °C are identical to our measurements for H_2SO_4-NH_3 particles between +5 °C and +20 °C at the same acid concentrations (*30*). The close agreement implies that the iodine oxoacid particles are growing at the dipole-dipole enhanced kinetic limit for HIO_3, with negligible evaporation at +10 °C or below. The measurements further indicate that HIO_3 dominates the growth of iodine particles in this size range and above (since the Kelvin barrier falls with increasing size). This behavior is in marked contrast with previous studies which considered that iodine oxides are responsible for growth (*10*, *27*). At -10 °C, the growth rate of HIO_3 particles increases by a further factor 2. This faster growth exceeds the kinetic limit for the arrival rate of HIO_3 monomers onto the particles and is attributed to additional growth from HIO_3 molecular clusters – similar to the situation for H_2SO_4-

DMA particles (*31*) – which provide a large pool of condensable material that is "hidden" from the HIO_3 monomer measurement.

Our nucleation and growth rate measurements (Fig. 1) indicate that HIO_3 concentrations above around 3×10^6 cm^{-3} and 1×10^7 cm^{-3} lead to rapid new particle formation at -10 °C and +10 °C, respectively. The survival probability of particles at low acid concentrations depends exponentially on the ratio of growth rate to condensation sink in the atmosphere, or wall-loss rate in a chamber. For CLOUD, the wall loss rate of sulfuric acid vapor is 2.2×10^{-3} s^{-1} (*30*), which is comparable to the condensation sink in the pristine continental boundary layer. In clean marine regions of the boundary layer or in the upper free troposphere, the condensation sink is often as low as 10^{-4}–10^{-5} s^{-1}. In such regions even lower HIO_3 concentrations will lead to sustained new particle formation and subsequent growth rates of a few 0.1 nm per hour. Under such conditions of extremely low HIO_3 concentrations and condensation sinks, it is likely that ions will be important to stabilize the embryonic clusters against evaporation, *i.e.* ion-induced nucleation will be the dominant mechanism.

Particle formation mechanisms

In Fig. 2 we show mass defect plots of negatively charged clusters (Fig. 2A) and neutral clusters (Fig. 2B) containing up to five iodine atoms, measured during nucleation events. The event in panel A) is continued in Fig. S3 up to clusters containing twelve iodine atoms. Fig. S4 shows all identified peaks of the event in panel B), before summing over water molecules and charger ions as displayed in Fig. 2B. Further details of the charged and neutral clusters and their signal strengths are provided in Table S2.

For ion-induced nucleation (Fig. 2A), we observe a sequence of negatively-charged iodine clusters of the form $(HIO_3)_{0\text{-}1}(I_2O_5)_n\cdot IO_3^-$, involving sequential addition of HIO_3 followed by rapid dehydration of $HIO_3\cdot HIO_3$ pairs in the cluster to form I_2O_5 (Fig. 3A), as previously observed at Mace Head (*11*). We find no nucleation occurs for positively charged iodine clusters (Fig. S5). This is clearly seen from the negative and positive charged particle spectra in Fig. S6; nucleation and growth only take place for negative particles. Almost all the negative particles have been neutralized by charge recombination before they reach 3 nm, and they continue to grow as mainly neutral particles. In Fig. 3A we provide a schematic representation of the mechanism for ion-induced iodic acid nucleation, interpreted from the mass defect plot (Fig. 2A).

Neutral nucleation of iodine oxoacid particles, however, proceeds by a different mechanism (Fig. 2B). We find that neutral HIO_3/I_2O_5 clusters are relatively weakly bound at these temperatures (none is detected above three iodine atoms). During neutral nucleation we observe repeated sequential addition of HIO_2 then HIO_3. The nucleating cluster sequences are shown schematically in Fig. 3B. A certain fraction of $HIO_3\cdot HIO_2$ pairs in the cluster dehydrate to form iodine tetroxide (I_2O_4, Fig. 3C). Since the three sequences shown in Fig. 3C have comparable intensities, it indicates the formation rate of I_2O_4 in the neutral clusters is comparable to the monomer collision rate (few 10^{-3} s^{-1}). In contrast, the strict conversion of $HIO_3\cdot HIO_3$ pairs during ion-induced nucleation (Fig. 3A) shows that the formation rate of I_2O_5 in the charged clusters is much faster than the monomer collision rate (few times 10^{-2} s^{-1}).

Our measurements show that HIO_2 plays a key role in stabilizing neutral HIO_3 clusters. To assess this, we used quantum chemistry to compute the formation free energy of several molecular dimers involving HIO_3 (Table S3 and Fig. S7). The most strongly bound dimer is $HIO_3 \cdot HIO_2$ (-12.9 kcal mol^{-1}). On the other hand, the $HIO_3 \cdot HIO_3$ (-7.7 kcal mol^{-1}) and $HIO_3 \cdot HOI$ (-1.6 kcal mol^{-1}) dimers are both less stable. This argues in favor of the dominant $HIO_3 \cdot HIO_2$ dimer shown in the 1→2 iodine step in Fig. 3B and not $HIO_3 \cdot HIO_3$ at the current experimental conditions. Our measurements and quantum chemical calculations suggest that HIO_2 stabilizes neutral HIO_3 clusters with a 1:1 stoichiometry similar to that seen for ammonia stabilization of embryonic H_2SO_4 clusters (*6*). For completeness, we note that, for neutral nucleation, we cannot exclude the direct addition of I_2O_4 molecules from gas phase I_2O_4, which we measure at concentrations of around 1% of HIO_3 (Table S2). We also note that HIO_3 shows very weak affinity for pairing with a base ($HIO_3 \cdot NH_3$ is -5.0 kcal mol^{-1}). Once the neutral particles exceed a critical size, they can continue to grow by condensation of HIO_3 alone (Fig. 1B), and so growth is no longer limited by the lower concentrations of HIO_2.

Ion-induced nucleation rate

To investigate ion-induced nucleation further, we have measured the collision rate coefficients, k_{i+1}, for each step in the process, $N_i^- + HIO_3 \rightarrow N_{i+1}^-$, where N_i^- represents a negatively charged cluster containing i iodine atoms (see He *et al.* (*32*), and Supplementary Materials for further details). The rate coefficients measured between neutral HIO_3 monomers and charged clusters containing up to 11 iodine atoms are shown in Fig. 4A. Within measurement errors, we find the same HIO_3 rate coefficient for each charged iodic cluster from the dimer to 11-mer, with a mean value [1.72 ±0.26 (stat.) +0.24/-0.21 (syst.)]$\times 10^{-9}$ cm^3 s^{-1} (1σ uncertainties). For comparison, we show the theoretical expectations for the rate coefficients for charged HIO_3 clusters from average dipole orientation theory (ADO, red curve) (*33*) and its extensions: hard-sphere average dipole orientation theory (HSA, green curve) and surface charged capture theory (SCC, blue curve) (*34*). The latter SCC theory agrees closely with our measurements. We show in Fig. 4B the enhancement factors for charged versus neutral rate coefficients (ratios of the CLOUD measurements divided by the neutral rate coefficients, ignoring dipole enhancement). The enhancement during ion-induced nucleation, which averages 6.3, rapidly shepherds newly formed particles through the smallest size range where they are highly mobile and most vulnerable to scavenging loss, and contributes to the faster particle formation rate.

Our measurements of the individual collision rate coefficients for charged clusters containing up to 11 iodine atoms (Fig. 4A) – and their good agreement with theoretical expectations – show that ion-induced iodic acid nucleation proceeds at the kinetic limit and therefore is strictly a barrierless process rather than nucleation. Significant evaporation of any cluster in this range would lead to a tell-tale higher apparent rate coefficient for the previous cluster. We have confirmed kinetic formation of charged clusters in two further ways. Firstly, we have used a kinetic model to calculate the ion-induced component of J_{gcr} *(*$= J_{iin} + J_n$*)* at +10 °C (see Supplementary Materials for details) and find it is consistent with our experimental measurements (Fig. 1A). Secondly, we have calculated the reaction free energies and evaporation rates for several molecular clusters containing an IO_3^- ion (Table S4). Our calculations show that extremely low evaporation rates are expected for charged iodine clusters. They further indicate that the $HIO_3 \cdot HIO_3 \cdot IO_3^-$ cluster is much less stable than $I_2O_5 \cdot IO_3^-$, supporting the sequence we observe experimentally in the first steps of

Fig. 3A. The HIO_3 collision rate measurements in Fig. 4A confirm that ion-induced nucleation is indeed due to the sequential addition of HIO_3 monomers and not, for example, to mixed accretion of HIO_3 and I_2O_5 molecules.

Particle composition

The measurements presented in Fig. 1B provide strong evidence that HIO_3 drives the growth of iodic particles above 1.8 nm. However, we have seen that additional iodine compounds play important roles during nucleation: HIO_2 for neutral nucleation, and the formation of iodine oxides – I_2O_5 and I_2O_4 – in the charged and neutral clusters, respectively (Fig. 2). To what extent do these other iodine species contribute to particle growth at larger sizes?

To address this question, we have directly measured the composition of freshly nucleated iodic particles in the size range up to around 10 nm with a soft-ionization Br^--FIGAERO (Filter Inlet for Gases and AEROsols) mass spectrometer. The majority (90%) of particles between 3 and 10 nm are neutral (Fig. S6). The FIGAERO collects particles on a Teflon filter for 30 min and then evaporates the sample with a controlled temperature ramp over the following 15 min at the inlet of a mass spectrometer. This measures the deposited mass of each chemical constituent of the particles and produces an individual "thermogram" of its volatility (evaporation temperature).

In Fig. 5A we show the evolution of particle size during a nucleation experiment. Particle sizes below 2.5 nm are measured by a PSM (Particle Size Magnifier) and above 4 nm by a nano-SMPS (Scanning Mobility Particle Sizer). In Fig. 5B we show the evolution of total particle volume derived from these measurements (blue circles). We also show in Fig. 5B the evolution of total HIO_3 volume concentration in the particle phase, measured by the FIGAERO. The mass spectrum is dominated by the single channel, HIO_3 (78% of the total mass, excluding water), with the rest being primarily I_2. We did not find a significant amount of HIO_2 in the particle-phase, due to its low concentration. The mass spectrum shows that the freshly formed particles are composed almost entirely of HIO_3, and not $I_2O_{4\text{-}5}$ as previously thought (*9–11*). This is independently confirmed by the close agreement seen in panel B) between the volume concentrations measured by the particle sizers and by the direct measurements of particulate HIO_3 with the FIGAERO. We have confirmed that the evaporated HIO_3 resulted from iodic acid in the particle phase – and not by thermal decomposition of other iodine compounds – by conducting laboratory calibrations. We nebulized iodic acid particles and then collected and analyzed them with the FIGAERO using the same procedures as for our experiments at CLOUD (see Supplementary Materials for details). The FIGAERO thermograms for the nebulized samples agree well with those obtained at CLOUD (Fig. S8).

Climate implications

Sulfuric acid-ammonia nucleation is known to be important in relatively pristine environments such as the free troposphere (*14*) or the Antarctic coastal region (*35*). We show here that the nucleation rate of iodine oxoacids exceeds $H_2SO_4 – NH_3$ at the same acid concentrations. In pristine, cooler regions of the atmosphere, HIO_3 concentrations above around 10^6 cm^{-3} will lead to copious new particle formation and sustained growth at a few times 0.1 nm per hour. The question then arises: are there pristine regions of the atmosphere where the concentrations of HIO_3 are

comparable to or exceed sulfuric acid, or else ammonia is absent? For those regions, HIO_3 could be the dominant source of new particles.

We show in Figs. S9 and S10 our global boundary layer measurements of HIO_3 at ten sites. The conditions for abundant iodine new particle formation and rapid growth are frequently reached at mid-latitude coastal sites with marine algae, such as Mace Head and Helsinki, at coastal polar sites such as Villum and Ny Ålesund in the Arctic, or Neumayer in the Antarctic. Although measurements over the remote ocean are sparse, frequent new particle formation over the high Arctic pack ice has recently been reported, driven by HIO_3 with little contribution from sulfuric acid (*36*).

The implications for the future are notable. Global iodine emissions have increased three-fold over the last 70 years and may continue to increase in the future as sea ice becomes thinner (*37*), and surface ozone increases (*18*). Any resultant increase of iodic CCN in the Arctic region could increase longwave radiative forcing from clouds and provide a positive feedback mechanism that accelerates the loss of sea ice. Iodine is also widespread in the free troposphere (*24*), where low temperatures, low condensation sinks, and high ion production rates from galactic cosmic rays favor iodic particle formation. Indeed, particulate iodate (IO_3^-) has recently been observed near the tropopause at iodine mixing ratios around 0.1-0.5 pptv, and IO_3^- is the main iodine reservoir in the stratosphere (*25*) (further discussion is provided in the Supplementary Materials).

In summary, our study shows that iodic acid, HIO_3, is the major iodine species driving both nucleation and growth of iodine oxoacid particles in the boundary layer, and it remains as the dominant constituent in the particulate phase. We have further shown that iodous acid, HIO_2, plays a key role in neutral nucleation by stabilizing HIO_3 clusters against evaporation – but is not important for particle growth at larger sizes. The efficacy of HIO_3 to form new particles exceeds the H_2SO_4 – NH_3 system at the same acid concentrations. Although atmospheric measurements remain limited, they are nevertheless sufficient to demonstrate the ubiquity of HIO_3 and its potential to compete with sulfuric acid(-ammonia) particle formation in pristine regions of the atmosphere such as marine coasts, the Arctic boundary layer or the upper free troposphere.

References and Notes:

1. H. Gordon, J. Kirkby, U. Baltensperger, F. Bianchi, M. Breitenlechner, J. Curtius, A. Dias, J. Dommen, N. M. Donahue, E. M. Dunne, J. Duplissy, S. Ehrhart, R. C. Flagan, C. Frege, C. Fuchs, A. Hansel, C. R. Hoyle, M. Kulmala, A. Kürten, K. Lehtipalo, V. Makhmutov, U. Molteni, M. P. Rissanen, Y. Stozkhov, J. Tröstl, G. Tsagkogeorgas, R. Wagner, C. Williamson, D. Wimmer, P. M. Winkler, C. Yan, K. S. Carslaw, Causes and importance of new particle formation in the present-day and preindustrial atmospheres. *Journal of Geophysical Research* **122**, 8739–8760 (2017).

2. G. A. Meehl, C. A. Senior, V. Eyring, G. Flato, J.-F. Lamarque, R. J. Stouffer, K. E. Taylor, M. Schlund, Context for interpreting equilibrium climate sensitivity and transient climate response from the CMIP6 Earth system models. *Science Advances*. **6**, eaba1981 (2020).

3. S. M. Kreidenweis, J. H. Seinfeld, Nucleation of sulfuric acid-water and methanesulfonic acid-water solution particles: implications for the atmospheric chemistry of organosulfur species. *Atmospheric Environment (1967)*. **22**, 283–296 (1988).

4. P. H. McMurry, M. Fink, H. Sakurai, M. R. Stolzenburg, R. L. Mauldin, J. Smith, F. Eisele, K. Moore, S. Sjostedt, D. Tanner, L. G. Huey, J. B. Nowak, E. Edgerton, D. Voisin, A criterion for new particle formation in the sulfur-rich Atlanta atmosphere. *Journal of Geophysical Research*. **110**, D22S02 (2005).

5. C. Kuang, P. H. McMurry, A. V. McCormick, F. L. Eisele, Dependence of nucleation rates on sulfuric acid vapor concentration in diverse atmospheric locations. *Journal of Geophysical Research*. **113**, D10209 (2008).

6. J. Kirkby, J. Curtius, J. Almeida, E. Dunne, J. Duplissy, S. Ehrhart, A. Franchin, S. Gagné, L. Ickes, A. Kürten, A. Kupc, A. Metzger, F. Riccobono, L. Rondo, S. Schobesberger, G. Tsagkogeorgas, D. Wimmer, A. Amorim, F. Bianchi, M. Breitenlechner, A. David, J. Dommen, A. Downard, M. Ehn, R. C. Flagan, S. Haider, A. Hansel, D. Hauser, W. Jud, H. Junninen, F. Kreissl, A. Kvashin, A. Laaksonen, K. Lehtipalo, J. Lima, E. R. Lovejoy, V. Makhmutov, S. Mathot, J. Mikkilä, P. Minginette, S. Mogo, T. Nieminen, A. Onnela, P. Pereira, T. Petäjä, R. Schnitzhofer, J. H. Seinfeld, M. Sipilä, Y. Stozhkov, F. Stratmann, A. Tomé, J. Vanhanen, Y. Viisanen, A. Vrtala, P. E. Wagner, H. Walther, E. Weingartner, H. Wex, P. M. Winkler, K. S. Carslaw, D. R. Worsnop, U. Baltensperger, M. Kulmala, Role of sulphuric acid, ammonia and galactic cosmic rays in atmospheric aerosol nucleation. *Nature*. **476**, 429–433 (2011).

7. M. Kulmala, J. Kontkanen, H. Junninen, K. Lehtipalo, H. E. Manninen, T. Nieminen, T. Petaja, M. Sipila, S. Schobesberger, P. Rantala, A. Franchin, T. Jokinen, E. Jarvinen, M. Aijala, J. Kangasluoma, J. Hakala, P. P. Aalto, P. Paasonen, J. Mikkila, J. Vanhanen, J. Aalto, H. Hakola, U. Makkonen, T. Ruuskanen, R. L. Mauldin, J. Duplissy, H. Vehkamaki, J. Back, A. Kortelainen, I. Riipinen, T. Kurten, M. V. Johnston, J. N. Smith, M. Ehn, T. F. Mentel, K. E. J. Lehtinen, A. Laaksonen, V.-M. Kerminen, D. R. Worsnop, Direct Observations of Atmospheric Aerosol Nucleation. *Science*. **339**, 943–946 (2013).

8. M. L. Dawson, M. E. Varner, V. Perraud, M. J. Ezell, R. B. Gerber, B. J. Finlayson-Pitts, Simplified mechanism for new particle formation from methanesulfonic acid, amines, and water via experiments and ab initio calculations. *Proceedings of the National Academy of Sciences*. **109**, 18719–18724 (2012).

9. T. Hoffmann, C. D. O'Dowd, J. H. Seinfeld, Iodine oxide homogeneous nucleation: An explanation for coastal new particle production. *Geophysical Research Letters*. **28**, 1949–1952 (2001).

10. C. D. O'Dowd, J. L. Jimenez, R. Bahreini, R. C. Flagan, J. H. Seinfeld, K. Hämeri, L. Pirjola, M. Kulmala, S. G. Jennings, T. Hoffmann, Marine aerosol formation from biogenic iodine emissions. *Nature*. **417**, 632–636 (2002).

11. M. Sipilä, N. Sarnela, T. Jokinen, H. Henschel, H. Junninen, J. Kontkanen, S. Richters, J. Kangasluoma, A. Franchin, O. Peräkylä, M. P. Rissanen, M. Ehn, H. Vehkamäki, T. Kurten, T. Berndt, T. Petäjä, D. Worsnop, D. Ceburnis, V.-M. Kerminen, M. Kulmala, C. O'Dowd, Molecular-scale evidence of aerosol particle formation via sequential addition of HIO_3. *Nature*. **537**, 532–534 (2016).

12. J. Kirkby, J. Duplissy, K. Sengupta, C. Frege, H. Gordon, C. Williamson, M. Heinritzi, M. Simon, C. Yan, J. Almeida, J. Trostl, T. Nieminen, I. K. Ortega, R. Wagner, A. Adamov, A. Amorim, A. K. Bernhammer, F. Bianchi, M. Breitenlechner, S. Brilke, X. M. Chen, J. Craven, A. Dias, S. Ehrhart, R. C. Flagan, A. Franchin, C. Fuchs, R. Guida, J. Hakala, C. R. Hoyle, T. Jokinen, H. Junninen, J. Kangasluoma, J. Kim, M. Krapf, A. Kurten, A. Laaksonen, K. Lehtipalo, V. Makhmutov, S. Mathot, U. Molteni, A. Onnela, O. Perakyla, F. Piel, T. Petaja, A. P. Praplan, K. Pringle, A. Rap, N. A. D. Richards, I. Riipinen, M. P. Rissanen, L. Rondo, N. Sarnela, S. Schobesberger, C. E. Scott, J. H. Seinfeld, M. Sipilä, G. Steiner, Y. Stozhkov, F. Stratmann, A. Tome, A. Virtanen, A. L. Vogel, A. C. Wagner, P. E. Wagner, E. Weingartner, D. Wimmer, P. M. Winkler, P. L. Ye, X. Zhang, A. Hansel, J. Dommen, N. M. Donahue, D. R. Worsnop, U. Baltensperger, M. Kulmala, K. S. Carslaw, J. Curtius, Ion-induced nucleation of pure biogenic particles. *Nature*. **533**, 521-526 (2016).

13. M. Wang, W. Kong, R. Marten, X.-C. He, D. Chen, J. Pfeifer, A. Heitto, J. Kontkanen, L. Dada, A. Kürten, T. Yli-Juuti, H. E. Manninen, S. Amanatidis, A. Amorim, R. Baalbaki, A. Baccarini, D. M. Bell, B. Bertozzi, S. Bräkling, S. Brilke, L. C. Murillo, R. Chiu, B. Chu, L.-P. De Menezes, J. Duplissy, H. Finkenzeller, L. G. Carracedo, M. Granzin, R. Guida, A. Hansel, V. Hofbauer, J. Krechmer, K. Lehtipalo, H. Lamkaddam, M. Lampimäki, C. P. Lee, V. Makhmutov, G. Marie, S. Mathot, R. L. Mauldin, B. Mentler, T. Müller, A. Onnela, E. Partoll, T. Petäjä, M. Philippov, V. Pospisilova, A. Ranjithkumar, M. Rissanen, B. Rörup, W. Scholz, J. Shen, M. Simon, M. Sipilä, G. Steiner, D. Stolzenburg, Y. J. Tham, A. Tomé, A. C. Wagner, D. S. Wang, Y. Wang, S. K. Weber, P. M. Winkler, P. J. Wlasits, Y. Wu, M. Xiao, Q. Ye, M. Zauner-Wieczorek, X. Zhou, R. Volkamer, I. Riipinen, J. Dommen, J. Curtius, U. Baltensperger, M. Kulmala, D. R. Worsnop, J. Kirkby, J. H. Seinfeld, I. El-Haddad, R. C. Flagan, N. M. Donahue, Rapid growth of new atmospheric particles by nitric acid and ammonia condensation. *Nature*. **581**, 184–189 (2020).

14. E. M. Dunne, H. Gordon, A. Kurten, J. Almeida, J. Duplissy, C. Williamson, I. K. Ortega, K. J. Pringle, A. Adamov, U. Baltensperger, P. Barmet, F. Benduhn, F. Bianchi, M. Breitenlechner, A. Clarke, J. Curtius, J. Dommen, N. M. Donahue, S. Ehrhart, R. C. Flagan, A. Franchin, R. Guida, J. Hakala, A. Hansel, M. Heinritzi, T. Jokinen, J. Kangasluoma, J. Kirkby, M. Kulmala, A. Kupc, M. J. Lawler, K. Lehtipalo, V. Makhmutov, G. Mann, S. Mathot, J. Merikanto, P. Miettinen, A. Nenes, A. Onnela, A. Rap, C. L. S. Reddington, F. Riccobono, N. A. D. Richards, M. P. Rissanen, L. Rondo, N. Sarnela, S. Schobesberger, K. Sengupta, M. Simon, M. Sipilä, J. N. Smith, Y. Stozkhov, A. Tome, J. Trostl, P. E. Wagner, D. Wimmer, P. M. Winkler, D. R. Worsnop, K. S. Carslaw, Global atmospheric particle formation from CERN CLOUD measurements. *Science*. **354**, 1119–1124 (2016).

15. J. Almeida, S. Schobesberger, A. Kürten, I. K. Ortega, O. Kupiainen-Määttä, A. P. Praplan, A. Adamov, A. Amorim, F. Bianchi, M. Breitenlechner, A. David, J. Dommen, N. M. Donahue, A. Downard, E. Dunne, J. Duplissy, S. Ehrhart, R. C. Flagan, A. Franchin, R. Guida, J. Hakala, A. Hansel, M. Heinritzi, H. Henschel, T. Jokinen, H. Junninen, M. Kajos, J. Kangasluoma, H. Keskinen, A. Kupc, T. Kurtén, A. N. Kvashin, A. Laaksonen, K. Lehtipalo, M. Leiminger, J. Leppä, V. Loukonen, V. Makhmutov, S. Mathot, M. J. McGrath, T. Nieminen, T. Olenius, A. Onnela, T. Petäjä, F. Riccobono, I. Riipinen, M. Rissanen, L. Rondo, T. Ruuskanen, F. D. Santos, N. Sarnela, S. Schallhart, R. Schnitzhofer, J. H. Seinfeld, M. Simon, M. Sipilä, Y. Stozhkov, F. Stratmann, A. Tomé, J. Tröstl, G. Tsagkogeorgas, P. Vaattovaara, Y. Viisanen, A. Virtanen, A. Vrtala, P. E. Wagner, E. Weingartner, H. Wex, C. Williamson, D. Wimmer, P. Ye, T. Yli-Juuti, K. S. Carslaw, M. Kulmala, J. Curtius, U. Baltensperger, D. R. Worsnop, H. Vehkamäki, J. Kirkby, Molecular understanding of sulphuric acid–amine particle nucleation in the atmosphere. *Nature*. **502**, 359–363 (2013).

16. R. J. Charlson, J. E. Lovelock, M. O. Andreae, S. G. Warren, Oceanic phytoplankton, atmospheric sulphur, cloud albedo and climate. *Nature*. **326**, 655–661 (1987).

17. T. M. Sherwen, M. J. Evans, D. V. Spracklen, L. J. Carpenter, R. Chance, A. R. Baker, J. A. Schmidt, T. J. Breider, Global modeling of tropospheric iodine aerosol. *Geophysical Research Letters*. **43**, 10012–10019 (2016).

18. L. J. Carpenter, S. M. MacDonald, M. D. Shaw, R. Kumar, R. W. Saunders, R. Parthipan, J. Wilson, J. M. C. Plane, Atmospheric iodine levels influenced by sea surface emissions of inorganic iodine. *Nature Geoscience*. **6**, 108–111 (2013).

19. A. S. Mahajan, J. M. C. Plane, H. Oetjen, L. Mendes, R. W. Saunders, A. Saiz-Lopez, C. E. Jones, L. J. Carpenter, G. B. McFiggans, Measurement and modelling of tropospheric reactive halogen species over the tropical Atlantic Ocean. *Atmospheric Chemistry and Physics*. **10**, 4611–4624 (2010).

20. B. C. Sive, R. K. Varner, H. Mao, D. R. Blake, O. W. Wingenter, R. Talbot, A large terrestrial source of methyl iodide. *Geophysical Research Letters*. **34** (2007).

21. J. D. Allan, P. I. Williams, J. Najera, J. D. Whitehead, M. J. Flynn, J. W. Taylor, D. Liu, E. Darbyshire, L. J. Carpenter, R. Chance, S. J. Andrews, S. C. Hackenberg, G. McFiggans, Iodine observed in new particle formation events in the Arctic atmosphere during ACCACIA. *Atmospheric Chemistry and Physics*. **15**, 5599–5609 (2015).

22. C. Prados-Roman, C. A. Cuevas, T. Hay, R. P. Fernandez, A. S. Mahajan, S.-J. Royer, M. Galí, R. Simó, J. Dachs, K. Großmann, D. E. Kinnison, J.-F. Lamarque, A. Saiz-Lopez, Iodine oxide in the global marine boundary layer. *Atmospheric Chemistry and Physics*. **15**, 583–593 (2015).

23. B. Dix, S. Baidar, J. F. Bresch, S. R. Hall, K. S. Schmidt, S. Wang, R. Volkamer, Detection of iodine monoxide in the tropical free troposphere. *Proceedings of the National Academy of Sciences*. **110**, 2035–40 (2013).

24. R. Volkamer, S. Baidar, T. L. Campos, S. Coburn, J. P. DiGangi, B. Dix, E. W. Eloranta, T. K. Koenig, B. Morley, I. Ortega, B. R. Pierce, M. Reeves, R. Sinreich, S. Wang, M. A. Zondlo, P. A. Romashkin, Aircraft measurements of BrO, IO, glyoxal, NO_2, H_2O, O_2-O_2 and aerosol extinction profiles in the tropics: Comparison with aircraft/ship-based in situ and lidar measurements. *Atmospheric Measurement Techniques*. **8**, 2121–2148 (2015).

25. T. K. Koenig, S. Baidar, P. Campuzano-Jost, C. A. Cuevas, B. Dix, R. P. Fernandez, H. Guo, S. R. Hall, D. Kinnison, B. A. Nault, K. Ullmann, J. L. Jimenez, A. Saiz-Lopez, R. Volkamer, Quantitative detection of iodine in the stratosphere. *Proceedings of the National Academy of Sciences*. **117**, 1860-1866 (2020).

26. H. Yu, L. Ren, X. Huang, M. Xie, J. He, H. Xiao, Iodine speciation and size distribution in ambient aerosols at a coastal new particle formation hotspot in China. *Atmospheric Chemistry and Physics*. **19**, 4025–4039 (2019).

27. J. C. Gómez Martín, T. R. Lewis, M. A. Blitz, J. M. C. Plane, M. Kumar, J. S. Francisco, A. Saiz-Lopez, A gas-to-particle conversion mechanism helps to explain atmospheric particle formation through clustering of iodine oxides. *Nature Communications*. **11**, 4521 (2020).

28. E. Drougas, A. M. Kosmas, Computational Studies of (HIO_3) Isomers and the HO_2 + IO Reaction Pathways. *The Journal of Physical Chemistry A*. **109**, 3887–3892 (2005).

29. J. M. C. Plane, D. M. Joseph, B. J. Allan, S. H. Ashworth, J. S. Francisco, An experimental and theoretical study of the reactions OIO + NO and OIO + OH. *Journal of Physical Chemistry A*. **110**, 93–100 (2006).

30. D. Stolzenburg, M. Simon, A. Ranjithkumar, A. Kürten, K. Lehtipalo, H. Gordon, S. Ehrhart, H. Finkenzeller, L. Pichelstorfer, T. Nieminen, X.-C. He, S. Brilke, M. Xiao, A. Amorim, R. Baalbaki, A. Baccarini, L. Beck, S. Bräkling, L. Caudillo Murillo, D. Chen, B. Chu, L. Dada, A. Dias, J. Dommen, J. Duplissy, I. El Haddad, L. Fischer, L. Gonzalez Carracedo, M. Heinritzi, C. Kim, T. K. Koenig, W. Kong, H. Lamkaddam, C. P. Lee, M. Leiminger, Z. Li, V. Makhmutov, H. E. Manninen, G. Marie, R. Marten, T. Müller, W. Nie, E. Partoll, T. Petäjä, J. Pfeifer, M. Philippov, M. P. Rissanen, B. Rörup, S. Schobesberger, S. Schuchmann, J. Shen, M. Sipilä, G. Steiner, Y. Stozhkov, C. Tauber, Y. J. Tham, A. Tomé, M. Vazquez-Pufleau, A. C. Wagner, M. Wang, Y. Wang, S. K. Weber, D. Wimmer, P. J. Wlasits, Y. Wu, Q. Ye, M. Zauner-Wieczorek, U. Baltensperger, K. S. Carslaw, J. Curtius, N. M. Donahue, R. C. Flagan, A. Hansel, M. Kulmala, J. Lelieveld, R. Volkamer, J. Kirkby, P. M. Winkler, Enhanced growth rate of atmospheric particles from sulfuric acid. *Atmospheric Chemistry and Physics*. **20**, 7359–7372 (2020).

31. K. Lehtipalo, L. Rondo, J. Kontkanen, S. Schobesberger, T. Jokinen, N. Sarnela, A. Kürten, S. Ehrhart, A. Franchin, T. Nieminen, F. Riccobono, M. Sipilä, T. Yli-Juuti, J. Duplissy, A. Adamov, L. Ahlm, J. Almeida, A. Amorim, F. Bianchi, M. Breitenlechner, J. Dommen, A. J. Downard, E. M. Dunne, R. C. Flagan, R. Guida, J.

Hakala, A. Hansel, W. Jud, J. Kangasluoma, V. M. Kerminen, H. Keskinen, J. Kim, J. Kirkby, A. Kupc, O. Kupiainen-Määttä, A. Laaksonen, M. J. Lawler, M. Leiminger, S. Mathot, T. Olenius, I. K. Ortega, A. Onnela, T. Petäjä, A. P. Praplan, M. P. Rissanen, T. M. Ruuskanen, F. D. Santos, S. Schallhart, R. Schnitzhofer, M. Simon, J. N. Smith, J. Tröstl, G. Tsagkogeorgas, A. Tomé, P. Vaattovaara, H. Vehkämäki, A. E. Vrtala, P. E. Wagner, C. Williamson, D. Wimmer, P. M. Winkler, A. Virtanen, N. M. Donahue, K. S. Carslaw, U. Baltensperger, I. Riipinen, J. Curtius, D. R. Worsnop, M. Kulmala, The effect of acid-base clustering and ions on the growth of atmospheric nano-particles. *Nature Communications*. **7**, 11594 (2016).

32. X.-C. He, S. Iyer, M. Sipilä, A. Ylisirniö, M. Peltola, J. Kontkanen, R. Baalbaki, M. Simon, A. Kürten, Y. J. Tham, J. Pesonen, L. R. Ahonen, S. Amanatidis, A. Amorim, A. Baccarini, L. Beck, F. Bianchi, S. Brilke, D. Chen, R. Chiu, J. Curtius, L. Dada, A. Dias, J. Dommen, N. M. Donahue, J. Duplissy, I. El Haddad, H. Finkenzeller, L. Fischer, M. Heinritzi, V. Hofbauer, J. Kangasluoma, C. Kim, T. K. Koenig, J. Kubečka, A. Kvashnin, H. Lamkaddam, C. P. Lee, M. Leiminger, Z. Li, V. Makhmutov, M. Xiao, R. Marten, W. Nie, A. Onnela, E. Partoll, T. Petäjä, V.-T. Salo, S. Schuchmann, G. Steiner, D. Stolzenburg, Y. Stozhkov, C. Tauber, A. Tomé, O. Väisänen, M. Vazquez-Pufleau, R. Volkamer, A. C. Wagner, M. Wang, Y. Wang, D. Wimmer, P. M. Winkler, D. R. Worsnop, Y. Wu, C. Yan, Q. Ye, K. Lehtinen, T. Nieminen, H. E. Manninen, M. Rissanen, S. Schobesberger, K. Lehtipalo, U. Baltensperger, A. Hansel, V.-M. Kerminen, R. C. Flagan, J. Kirkby, T. Kurtén, M. Kulmala, Determination of the collision rate coefficient between charged iodic acid clusters and iodic acid using the appearance time method. *Aerosol Science and Technology*. *null*, 1–12 (2020).

33. T. Su, M. T. Bowers, Theory of ion-polar molecule collisions. Comparison with experimental charge transfer reactions of rare gas ions to geometric isomers of difluorobenzene and dichloroethylene. *The Journal of Chemical Physics*. **58**, 3027–3037 (1973).

34. G. Kummerlöwe, M. K. Beyer, Rate estimates for collisions of ionic clusters with neutral reactant molecules. *International Journal of Mass Spectrometry*. **244**, 84–90 (2005).

35. T. Jokinen, M. Sipilä, J. Kontkanen, V. Vakkari, P. Tisler, E.-M. Duplissy, H. Junninen, J. Kangasluoma, H. E. Manninen, T. Petäjä, M. Kulmala, D. R. Worsnop, J. Kirkby, A. Virkkula, V.-M. Kerminen, Ion-induced sulfuric acid–ammonia nucleation drives particle formation in coastal Antarctica. *Science Advances*. **4**, eaat9744 (2018).

36. A. Baccarini, L. Karlsson, J. Dommen, P. Duplessis, J. Vüllers, I. M. Brooks, A. Saiz-Lopez, M. Salter, M. Tjernström, U. Baltensperger, P. Zieger, J. Schmale, Frequent new particle formation over the high Arctic pack ice by enhanced iodine emissions. *Nature Communications*. **11**, 4924 (2020).

37. C. A. Cuevas, N. Maffezzoli, J. P. Corella, A. Spolaor, P. Vallelonga, H. A. Kjær, M. Simonsen, M. Winstrup, B. Vinther, C. Horvat, R. P. Fernandez, D. Kinnison, J.-F. Lamarque, C. Barbante, A. Saiz-Lopez, Rapid increase in atmospheric iodine levels in the North Atlantic since the mid-20th century. *Nature Communications*. **9**, 1452 (2018)

38. X.-C. He, Y. J. Tham, L. Dada, M. Wang, H. Finkenzeller, D. Stolzenburg, S. Iyer, M. Simon, A. Kürten, J. Shen, B. Rörup, M. Rissanen, S. Schobesberger, R. Baalbaki, D. S. Wang, T. K. Koenig, T. Jokinen, N. Sarnela, L. Beck, J. Almeida, S. Amanatidis, A. Amorim, F. Ataei, A. Baccarini, B. Bertozzi, F. Bianchi, S. Brilke, L. Caudillo, D. Chen, R. Chiu, B. Chu, A. Dias, A. Ding, J. Dommen, J. Duplissy, I. El Haddad, L. Gonzalez Carracedo, M. Granzin, A. Hansel, M. Heinritzi, V. Hofbauer, H. Junninen, J. Kangasluoma, D. Kemppainen, C. Kim, W. Kong, J. E. Krechmer, A. Kvashnin, T. Laitinen, H. Lamkaddam, C. P. Lee, K. Lehtipalo, M. Leiminger, Z. Li, V. Makhmutov, H. E. Manninen, G. Marie, R. Marten, S. Mathot, R. L. Mauldin, B. Mentler, O. Möhler, T. Müller, W. Nie, A. Onnela, T. Petäjä, J. Pfeifer, M. Philippov, A. Ranjithkumar, A. Saiz-Lopez, I. Salma, W. Scholz, S. Schuchmann, B. Schulze, G. Steiner, Y. Stozhkov, C. Tauber, A. Tomé, R. C. Thakur, O. Väisänen, M. Vazquez-Pufleau, A. C. Wagner, Y. Wang, S. K. Weber, P. M. Winkler, Y. Wu, M. Xiao, C. Yan, Q. Ye, A. Ylisirniö, M. Zauner-Wieczorek, Q. Zha, P. Zhou, R. C. Flagan, J. Curtius, U. Baltensperger, M. Kulmala, V.-M. Kerminen, T. Kurtén, N. M. Donahue, R. Volkamer, J. Kirkby, D. R. Worsnop, M. Sipilä, Role of iodine oxoacids in atmospheric aerosol nucleation: data resources (2021), doi:10.5281/zenodo.4299441.

39. J. Duplissy, J. Merikanto, A. Franchin, G. Tsagkogeorgas, J. Kangasluoma, D. Wimmer, H. Vuollekoski, S. Schobesberger, K. Lehtipalo, R. C. Flagan, D. Brus, N. M. Donahue, H. Vehkamäki, J. Almeida, A. Amorim, P. Barmet, F. Bianchi, M. Breitenlechner, E. M. Dunne, R. Guida, H. Henschel, H. Junninen, J. Kirkby, A. Kürten, A. Kupc, A. Määttänen, V. Makhmutov, S. Mathot, T. Nieminen, A. Onnela, A. P. Praplan, F. Riccobono, L. Rondo, G. Steiner, A. Tome, H. Walther, U. Baltensperger, K. S. Carslaw, J. Dommen, A. Hansel, T. Petäjä, M. Sipilä, F. Stratmann, A. Vrtala, P. E. Wagner, D. R. Worsnop, J. Curtius, M. Kulmala, Effect of ions on sulfuric acid-water binary particle formation: 2. Experimental data and comparison with QC-normalized classical nucleation theory. *Journal of Geophysical Research*. **121**, 1752–1775 (2016).

40. F. D. Lopez-Hilfiker, C. Mohr, M. Ehn, F. Rubach, E. Kleist, J. Wildt, T. F. Mentel, A. Lutz, M. Hallquist, D. Worsnop, J. A. Thornton, A novel method for online analysis of gas and particle composition: description and evaluation of a Filter Inlet for Gases and AEROsols (FIGAERO). *Atmospheric Measurement Techniques*. **7**, 983–1001 (2014).

41. H. Junninen, M. Ehn, Petäjä, L. Luosujärvi, T. Kotiaho, R. Kostiainen, U. Rohner, M. Gonin, K. Fuhrer, M. Kulmala, D. R. Worsnop, A high-resolution mass spectrometer to measure atmospheric ion composition. *Atmospheric Measurement Techniques*. **3**, 1039–1053 (2010).

42. T. Jokinen, M. Sipilä, H. Junninen, M. Ehn, G. Lönn, J. Hakala, T. Petäjä, R. L. Mauldin, M. Kulmala, D. R. Worsnop, Atmospheric sulphuric acid and neutral cluster measurements using CI-APi-TOF. *Atmospheric Chemistry and Physics*. **12**, 4117–4125 (2012).

43. A. Kürten, T. Jokinen, M. Simon, M. Sipilä, N. Sarnela, H. Junninen, A. Adamov, J. Almeida, A. Amorim, F. Bianchi, M. Breitenlechner, J. Dommen, N. M. Donahue, J. Duplissy, S. Ehrhart, R. C. Flagan, A. Franchin, J. Hakala, A. Hansel, M. Heinritzi, M. Hutterli, J. Kangasluoma, J. Kirkby, A. Laaksonen, K. Lehtipalo, M. Leiminger, V. Makhmutov, S. Mathot, A. Onnela, T. Petäjä, A. P. Praplan, F. Riccobono, M. P. Rissanen, L. Rondo, S. Schobesberger, J. H. Seinfeld, G. Steiner, A. Tomé, J. Tröstl, P. M. Winkler, C. Williamson, D. Wimmer, P. Ye, U. Baltensperger, K. S. Carslaw, M. Kulmala, D. R. Worsnop, J. Curtius, Neutral molecular cluster formation of sulfuric acid–dimethylamine observed in real time under atmospheric conditions. *Proceedings of the National Academy of Sciences*. **111**, 15019–15024 (2014).

44. R. A. Washenfelder, A. O. Langford, H. Fuchs, S. S. Brown, Measurement of glyoxal using an incoherent broadband cavity enhanced absorption spectrometer. *Atmospheric Chemistry and Physics*. **8**, 7779-7793 (2008).

45. R. Thalman, R. Volkamer, Temperature dependent absorption cross-sections of O_2–O_2 collision pairs between 340 and 630 nm and at atmospherically relevant pressure. *Physical Chemistry Chemical Physics*. **15**, 15371 (2013).

46. J. Vanhanen, J. Mikkilä, K. Lehtipalo, M. Sipilä, H. E. Manninen, E. Siivola, T. Petäjä, M. Kulmala, Particle Size Magnifier for Nano-CN Detection. *Aerosol Science and Technology*. **45**, 533–542 (2011).

47. H. E. Manninen, S. Mirme, A. Mirme, T. Petäjä, M. Kulmala, How to reliably detect molecular clusters and nucleation mode particles withNeutral cluster and Air Ion Spectrometer (NAIS). *Atmospheric Measurement Techniques*. **9**, 3577–3605 (2016).

48. D. Stolzenburg, G. Steiner, P. M. Winkler, A DMA-train for precision measurement of sub-10 nm aerosol dynamics. *Atmospheric Measurement Techniques*. **10**, 1639–1651 (2017).

49. J. Tröstl, T. Tritscher, O. F. Bischof, H.-G. Horn, T. Krinke, U. Baltensperger, M. Gysel, Fast and precise measurement in the sub-20nm size range using a Scanning Mobility Particle Sizer. *Journal of Aerosol Science*. **87**, 75–87 (2015).

50. K. Lehtipalo, C. Yan, L. Dada, F. Bianchi, M. Xiao, R. Wagner, D. Stolzenburg, L. R. Ahonen, A. Amorim, A. Baccarini, P. S. Bauer, B. Baumgartner, A. Bergen, A.-K. Bernhammer, M. Breitenlechner, S. Brilke, A. Buchholz, S. B. Mazon, D. Chen, X. Chen, A. Dias, J. Dommen, D. C. Draper, J. Duplissy, M. Ehn, H. Finkenzeller, L. Fischer, C. Frege, C. Fuchs, O. Garmash, H. Gordon, J. Hakala, X. He, L. Heikkinen, M.

Heinritzi, J. C. Helm, V. Hofbauer, C. R. Hoyle, T. Jokinen, J. Kangasluoma, V.-M. Kerminen, C. Kim, J. Kirkby, J. Kontkanen, A. Kürten, M. J. Lawler, H. Mai, S. Mathot, R. L. Mauldin, U. Molteni, L. Nichman, W. Nie, T. Nieminen, A. Ojdanic, A. Onnela, M. Passananti, T. Petäjä, F. Piel, V. Pospisilova, L. L. J. Quéléver, M. P. Rissanen, C. Rose, N. Sarnela, S. Schallhart, S. Schuchmann, K. Sengupta, M. Simon, M. Sipilä, C. Tauber, A. Tomé, J. Tröstl, O. Väisänen, A. L. Vogel, R. Volkamer, A. C. Wagner, M. Wang, L. Weitz, D. Wimmer, P. Ye, A. Ylisirniö, Q. Zha, K. S. Carslaw, J. Curtius, N. M. Donahue, R. C. Flagan, A. Hansel, I. Riipinen, A. Virtanen, P. M. Winkler, U. Baltensperger, M. Kulmala, D. R. Worsnop, Multicomponent new particle formation from sulfuric acid, ammonia, and biogenic vapors. *Science Advances* **4**, eaau5363 (2018).

51. K. Lehtipalo, J. Leppa, J. Kontkanen, J. Kangasluoma, A. Franchin, D. Wimnner, S. Schobesberger, H. Junninen, T. Petaja, M. Sipila, Methods for determining particle size distribution and growth rates between 1 and 3 nm using the Particle Size Magnifier. *Boreal Environment Research* (2014).

52. M. J. Frisch, G. W. Trucks, H. B. Schlegel, G. E. Scuseria, M. A. Robb, J. R. Cheeseman, G. Scalmani, V. Barone, B. Mennucci, G. A. Petersson, H. Nakatsuji, M. Caricato, X. Li, H. P. Hratchian, A. F. Izmaylov, J. Bloino, G. Zheng, J. L. Sonnenberg, M. Hada, M. Ehara, K. Toyota, R. Fukuda, J. Hasegawa, M. Ishida, T. Nakajima, Y. Honda, O. Kitao, H. Nakai, T. Vreven, J. A. Montgomery, J. E. Peralta, F. Ogliaro, M. Bearpark, J. J. Heyd, E. Brothers, K. N. Kudin, V. N. Staroverov, R. Kobayashi, J. Normand, K. Raghavachari, A. Rendell, J. C. Burant, S. S. Iyengar, J. Tomasi, M. Cossi, N. Rega, J. M. Millam, M. Klene, J. E. Knox, J. B. Cross, V. Bakken, C. Adamo, J. Jaramillo, R. Gomperts, R. E. Stratmann, O. Yazyev, A. J. Austin, R. Cammi, C. Pomelli, J. W. Ochterski, R. L. Martin, K. Morokuma, V. G. Zakrzewski, G. A. Voth, P. Salvador, J. J. Dannenberg, S. Dapprich, A. D. Daniels, Farkas, J. B. Foresman, J. V. Ortiz, J. Cioslowski, D. J. Fox, *Gaussian 09, Revision D.01* (Gaussian, Inc., Wallingford CT, 2009).

53. J. Zhang, M. Dolg, ABCluster: the artificial bee colony algorithm for cluster global optimization. *Physical Chemistry Chemical Physics*. **17**, 24173–24181 (2015).

54. J. Zhang, M. Dolg, Global optimization of clusters of rigid molecules using the artificial bee colony algorithm. *Physical Chemistry Chemical Physics*. **18**, 3003–3010 (2016).

55. K. Vanommeslaeghe, E. Hatcher, C. Acharya, S. Kundu, S. Zhong, J. Shim, E. Darian, O. Guvench, P. Lopes, I. Vorobyov, A. D. Mackerell, *Journal of Computational Chemistry*. **31**, *671-690* (2009).

56. N. Hyttinen, R. V. Otkjær, S. Iyer, H. G. Kjaergaard, M. P. Rissanen, P. O. Wennberg, T. Kurtén, Computational Comparison of Different Reagent Ions in the Chemical Ionization of Oxidized Multifunctional Compounds. *Journal of Physical Chemistry A*. **122**, 269–279 (2018).

57. D. Feller, The role of databases in support of computational chemistry calculations. *Journal of Computational Chemistry*. **17**, 1571–1586 (1996).

58. R. A. Kendall, T. H. Dunning, R. J. Harrison, Electron affinities of the first-row atoms revisited. Systematic basis sets and wave functions. *The Journal of Chemical Physics*. **96**, 6796–6806 (1992).

59. C. Riplinger, F. Neese, An efficient and near linear scaling pair natural orbital based local coupled cluster method. *The Journal of Chemical Physics*. **138**, 034106 (2013).

60. F. Neese, The ORCA program system: The ORCA program system. *Wiley Interdisciplinary Reviews: Computational Molecular Science*. **2**, 73–78 (2012).

61. A. Kürten, C. Li, F. Bianchi, J. Curtius, A. Dias, N. M. Donahue, J. Duplissy, R. C. Flagan, J. Hakala, T. Jokinen, J. Kirkby, M. Kulmala, A. Laaksonen, K. Lehtipalo, V. Makhmutov, A. Onnela, M. P. Rissanen, M. Simon, M. Sipilä, Y. Stozhkov, J. Tröstl, P. Ye, P. H. McMurry, New particle formation in the sulfuric acid–dimethylamine–water system: reevaluation of CLOUD chamber measurements and comparison to an aerosol nucleation and growth model. *Atmospheric Chemistry and Physics*. **18**, 845–863 (2018).

62. A. Kürten, New particle formation from sulfuric acid and ammonia: nucleation and growth model based on thermodynamics derived from CLOUD measurements for a wide range of conditions. *Atmospheric Chemistry and Physics*. **19**, 5033–5050 (2019).

63. S. Khanniche, F. Louis, L. Cantrel, I. Černušák, A theoretical study of the microhydration of iodic acid ($HOIO_2$). *Computational and Theoretical Chemistry*. **1094**, 98–107 (2016).

64. P. Hari, E. Nikinmaa, T. Pohja, E. Siivola, J. Bäck, T. Vesala, M. Kulmala, Station for measuring ecosystem-atmosphere relations: SMEAR. *Physical and Physiological Forest Ecology*. **9789400756**, 471–487 (2013).

65. Y. Zhou, L. Dada, Y. Liu, Y. Fu, J. Kangasluoma, T. Chan, C. Yan, B. Chu, K. R. Daellenbach, F. Bianchi, T. Kokkonen, Y. Liu, J. Kujansuu, V.-M. Kerminen, T. Petäjä, L. Wang, J. Jiang, M. Kulmala, Variation of size-segregated particle number concentrations in winter Beijing. *Atmospheric Chemistry and Physics* **20**, 1201-1216 (2020).

66. C. Deng, Y. Fu, L. Dada, C. Yan, R. Cai, D. Yang, Y. Zhou, R. Yin, Y. Lu, X. Li, X. Qiao, X. Fan, W. Nie, J. Kontkanen, J. Kangasluoma, B. Chu, A. Ding, V.-M. Kerminen, P. Paasonen, D. R. Worsnop, F. Bianchi, Y. Liu, J. Zheng, L. Wang, M. Kulmala, J. Jiang, Seasonal Characteristics of New Particle Formation and Growth in Urban Beijing. *Environ. Sci. Technol.* **54**, 8547–8557 (2020).

67. T. Hussein, J. Martikainen, H. Junninen, L. Sogacheva, R. Wagner, M. D. Maso, I. Riipinen, P. P. Aalto, M. Kulmala, Observation of regional new particle formation in the urban atmosphere. *Tellus B: Chemical and Physical Meteorology*. **60**, 509–521 (2008).

68. S. Wang, J. A. Schmidt, S. Baidar, S. Coburn, B. Dix, T. K. Koenig, E. Apel, D. Bowdalo, T. L. Campos, E. Eloranta, M. J. Evans, J. P. DiGangi, M. A. Zondlo, R.-S. Gao, J. A. Haggerty, S. R. Hall, R. S. Hornbrook, D. Jacob, B. Morley, B. Pierce, M. Reeves, P. Romashkin, A. Ter Schure, R. Volkamer, Active and widespread halogen chemistry in the tropical and subtropical free troposphere. *Proceedings of the National Academy of Sciences*. **112**, 9281–6 (2015).

69. A. Saiz-Lopez, S. Baidar, C. A. Cuevas, T. K. Koenig, R. P. Fernandez, B. Dix, D. E. Kinnison, J. -F. Lamarque, X. Rodriguez-Lloveras, T. L. Campos, R. Volkamer, Injection of iodine to the stratosphere. *Geophysical Research Letters*. **42**, 6852–6859 (2015).

70. I. Pundt, J.-P. Pommereau, C. Phillips, E. Lateltin, Upper Limit of Iodine Oxide in the Lower Stratosphere. *Journal of Atmospheric Chemistry*. **30**, 173–185 (1998).

71. H. Bösch, Upper limits of stratospheric IO and OIO inferred from center-to-limb-darkening-corrected balloon-borne solar occultation visible spectra: Implications for total gaseous iodine and stratospheric ozone. *Journal of Geophysical Research* **108**, 4455 (2003).

72. Yu. I. Stozhkov, N. S. Svirzhevsky, G. A. Bazilevskaya, A. N. Kvashnin, V. S. Makhmutov, A. K. Svirzhevskaya, Long-term (50 years) measurements of cosmic ray fluxes in the atmosphere. *Advances in Space Research*. **44**, 1124–1137 (2009).

73. C. J. Williamson, A. Kupc, D. Axisa, K. R. Bilsback, T. Bui, P. Campuzano-Jost, M. Dollner, K. D. Froyd, A. L. Hodshire, J. L. Jimenez, J. K. Kodros, G. Luo, D. M. Murphy, B. A. Nault, E. A. Ray, B. Weinzierl, J. C. Wilson, F. Yu, P. Yu, J. R. Pierce, C. A. Brock, A large source of cloud condensation nuclei from new particle formation in the tropics. *Nature*. **574**, 399–403 (2019).

74. D. L. Hartmann, L. A. Moy, Q. Fu, Tropical Convection and the Energy Balance at the Top of the Atmosphere. *Journal of Climate*. **14**, 17 (2001).

75. A. Gettelman, Radiation balance of the tropical tropopause layer. *Journal of Geophysical Research*. **109**, D07103 (2004).

76. M. Legrand, J. R. McConnell, S. Preunkert, M. Arienzo, N. Chellman, K. Gleason, T. Sherwen, M. J. Evans, L. J. Carpenter, Alpine ice evidence of a three-fold increase in atmospheric iodine deposition since 1950 in Europe due to increasing oceanic emissions. *Proceedings of the National Academy of Sciences*. **115**, 12136–12141 (2018).

77. X. Zhao, X. Hou, W. Zhou, Atmospheric Iodine (^{127}I and ^{129}I) Record in Spruce Tree Rings in the Northeast Qinghai-Tibet Plateau. *Environmental Science and Technology*. **15**, 8706-8714 (2019)

78. S. Khanniche, F. Louis, L. Cantrel, I. Černušák, Computational study of the $I_2O_5+H_2O=2HOIO_2$ gas-phase reaction. *Chemical Physics Letters*. **662**, 114–119 (2016).

79. M. Passananti, E. Zapadinsky, T. Zanca, J. Kangasluoma, N. Myllys, M. P. Rissanen, T. Kurtén, M. Ehn, M. Attoui, H. Vehkamäki, How well can we predict cluster fragmentation inside a mass spectrometer? *Chemical Communications* **55**, 5946–5949 (2019).

80. R. J. Huang, K. Seitz, J. Buxmann, D. Pöhler, K. E. Hornsby, L. J. Carpenter, U. Platt, T. Hoffmann, In situ measurements of molecular iodine in the marine boundary layer: The link to macroalgae and the implications for O_3, IO, OIO and NO_x. *Atmospheric Chemistry and Physics*. **10**, 4823–4833 (2010).

81. A. Saiz-Lopez, R. W. Saunders, D. M. Joseph, S. H. Ashworth, J. M. C. Plane, Absolute absorption cross-section and photolysis rate of I_2. *Atmospheric Chemistry and Physics*. **4**, 1443–1450 (2004).

Funding: We thank the European Organization for Nuclear Research (CERN) for supporting CLOUD with important technical and financial resources and for providing a particle beam from the CERN Proton Synchrotron. This research has received support from the Academy of Finland projects (316114, 307331, 310682, 266388, 3282290, 306853, 296628, 229574, 326948, 1325656); The European Research Council projects (692891, 616075, 764991, 316662, 742206, 714621); CSC – Finnish IT center; the EC Seventh Framework Programme and the EU H2020 programme Marie Skłodowska Curie ITN "CLOUD-TRAIN" (no. 316662) and "CLOUD-MOTION" (no. 764991); Austrian Science fund (FWF, J3951-N36, P27295-N20); the Swiss National Science Foundation (20FI20_159851, 200021_169090, 200020_172602, 20FI20_172622); the U.S. National Science Foundation Grants (AGS1447056, AGS1439551, AGS1801574, AGS1620530, AGS1801897, AGS153128, AGS1649147, AGS1801280, AGS1602086, AGS1801329); MSCA H2020 COFUND-FP-CERN-2014 fellowship (665779); German Federal Ministry of Education and Research: CLOUD-16 (01LK1601A); Portuguese Foundation for Science and Technology (CERN/FIS-COM/0014/2017); Academy of Finland Centre of Excellence in Atmospheric Sciences (grant no. 272041); European Regional Development Fund project (MOBTT42); Estonian Research Council project (PRG714); Hungarian National Research, Development and Innovation Office (K116788, K132254); NASA Graduate Fellowship (NASA-NNX16AP36H); ACTRIS 2TNA H2020 OCTAVE (654109). We are also grateful for all the people who have contributed to the field measurements around the world. **Author Contributions:** X.-C.H., M.K., J.Ki., M.Sip. planned the experiments. X.-C.H., Y.J.T., L.D., M.W., H.F., D.S., M.Sim., A.Kü., J.S., B.R., S.I., M.R., S.Scho., R.B., D.S.W., T.K.K., S.A., A.A., A.B., S.B., L.C., D.C., B.C. A.Dias, J.Du., I.E.H., R.C.F., L.G.C., M.G., M.H., V.H., H.J., J.Ka., D.K., C.K., W.K., J.E.K., A.Kv., T.L., H.L., C.P.L., K.L., M.L., Z.L., V.M., H.E.M., G.M., R.M., R.L.M., B.M., O.M., T.M., A.O., T.P., J.P., M.P., W.S., S.Schu., B.S., G.S., Y.S., A.T., M.V.-P., A.C.W., S.K.W., W.N., P.M.W., Y.Wu, A.Y., Y.Wang, M.Z.-W., Q.Z., J.C., M.K., U.B., R.V., J.Ki., and M.Sip. prepared the CLOUD facility or measuring instruments. X.-C.H., Y.J.T., L.D., M.W., H.F., D.S., M.Sim., J.S., B.R., M.R., R.B., D.S.W., T.K.K., T.J., N.S., L.B., F.A., A.B., F.B., B.B., S.B., D.C., R.C., A.Ding, J.Du., L.G.C., M.G., M.H., V.H., H.J., D.K., C.K., J.E.K., H.L., C.P.L., M.L., Z.L., H.E.M., G.M., R.M., R.L.M., B.M., T.M., J.P., A.R., I.S., S.Schu., B.S., G.S., C.T., A.T., R.C.T., O.V., M.V.-P., A.C.W., S.K.W., W.N., Y.Wu, M.X., C.Y., Q.Y., A.Y., Y.Wang, M.Z.-W., R.V., and J.Ki. collected the data. X.-C.H., Y.J.T., L.D., M.W., H.F., D.S., M.Sim., J.S., B.R., R.C.F., D.K., C.K., W.K., S.K.W., P.M.W., P.Z., T.K., R.V., and D.R.W. analyzed the data. J.Ki and X.-C.H. wrote the manuscript with contributions from R.V., Y.J.T., M.W., H.F., T.K.K, M.K., T.K., N.M.D., D.R.W. and M.Sip. X.-C.H., Y.J.T., L.D., M.W., H.F., D.S., B.R., S.I., M.R., S.Scho., R.B., T.K.K., N.S., A.B., A.Ding, J.Do., J.Du., I.E.H., A.H., H.J., J.Ka., J.E.K., H.L., C.P.L., K.L., R.L.M., B.M., O.M., T.P., A.S.-L., I.S., P.Z., J.C., U.B., M.K., V.-M.K., T.K., N.M.D., R.V., J.Ki., D.R.W. and M.Sip. commented and edited on the manuscript. **Competing interest:** the authors declare no competing interest. **Data and materials availability:** Data for all figures in the main text and Supplementary Materials are available at the Zenodo repository (DOI: 10.5281/zenodo.4299441).

Supplementary Materials:

Materials and methods

Supplementary text

Tables S1-S4

Figures S1-S10

References (*39-81*)

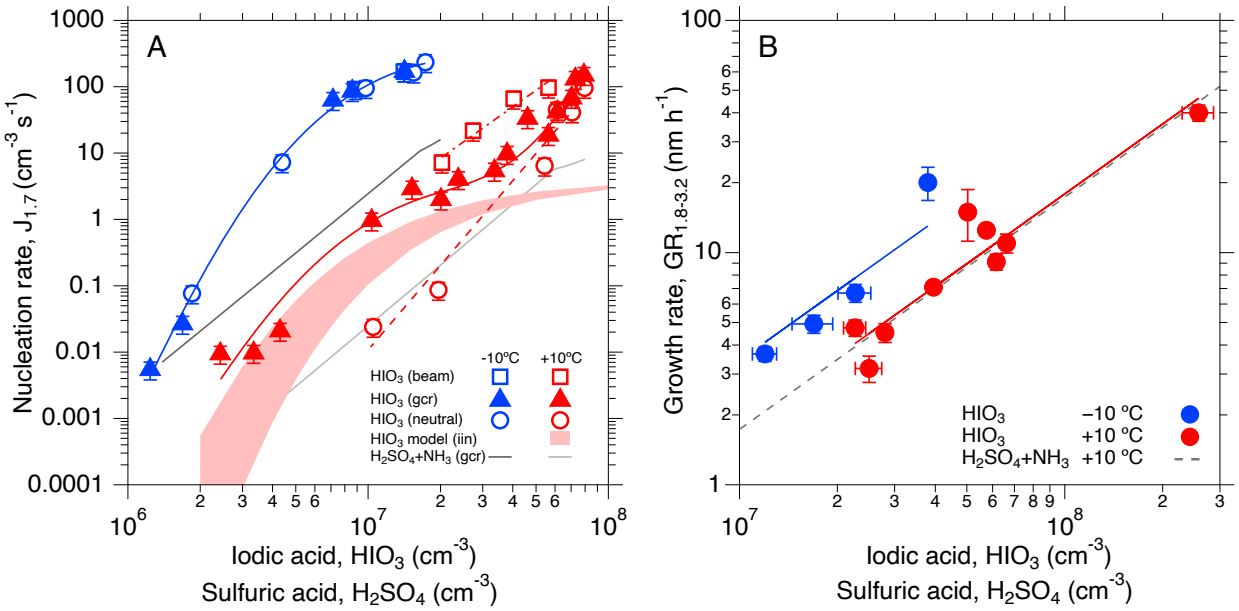

Fig. 1. Nucleation and growth rates versus iodic acid concentration. A) Nucleation rates at 1.7 nm diameter versus iodic acid concentration at +10 °C (red symbols and curves) and -10 °C (blue symbols and curves). Hollow circles show the nucleation rates for neutral conditions, J_n, solid triangles for gcr conditions, J_{gcr}, and hollow squares for beam conditions, J_{beam}. To guide the eye, the measurements are connected by approximate curves. The red band shows a kinetic model prediction for HIO_3 ion-induced nucleation, J_{iin} *(=* $J_{gcr} - J_n$*),* at +10 °C (see Supplementary Materials for further details). The lower and upper limits correspond, respectively, to zero and two H_2O molecules per iodine atom in the cluster. For comparison, the gcr nucleation rates measured for sulfuric acid with 100 pptv ammonia are shown at +10 °C (light grey curve) and -10 °C (dark grey curve) (*14*). B) Mean growth rates of particles (neutral, gcr and beam) between 1.8 nm and 3.2 nm diameter versus HIO_3 concentration at +10 °C (filled red circles) and -10 °C (filled blue circles). For comparison, the dashed grey line shows the growth rates of H_2SO_4-NH_3 particles measured at +10 °C (*30*). The bars in both panels represent $\pm 1\sigma$ measurement errors. The experimental conditions are 36-44 ppbv O_3, 34-73% relative humidity (RH), 0.4-168 pptv I_2 and an I atom production rate of 4.4×10^4-1.5×10^7 $cm^{-3}s^{-1}$. An overall systematic scale error on the HIO_3 concentration of -33%/+50% is not shown on the data points.

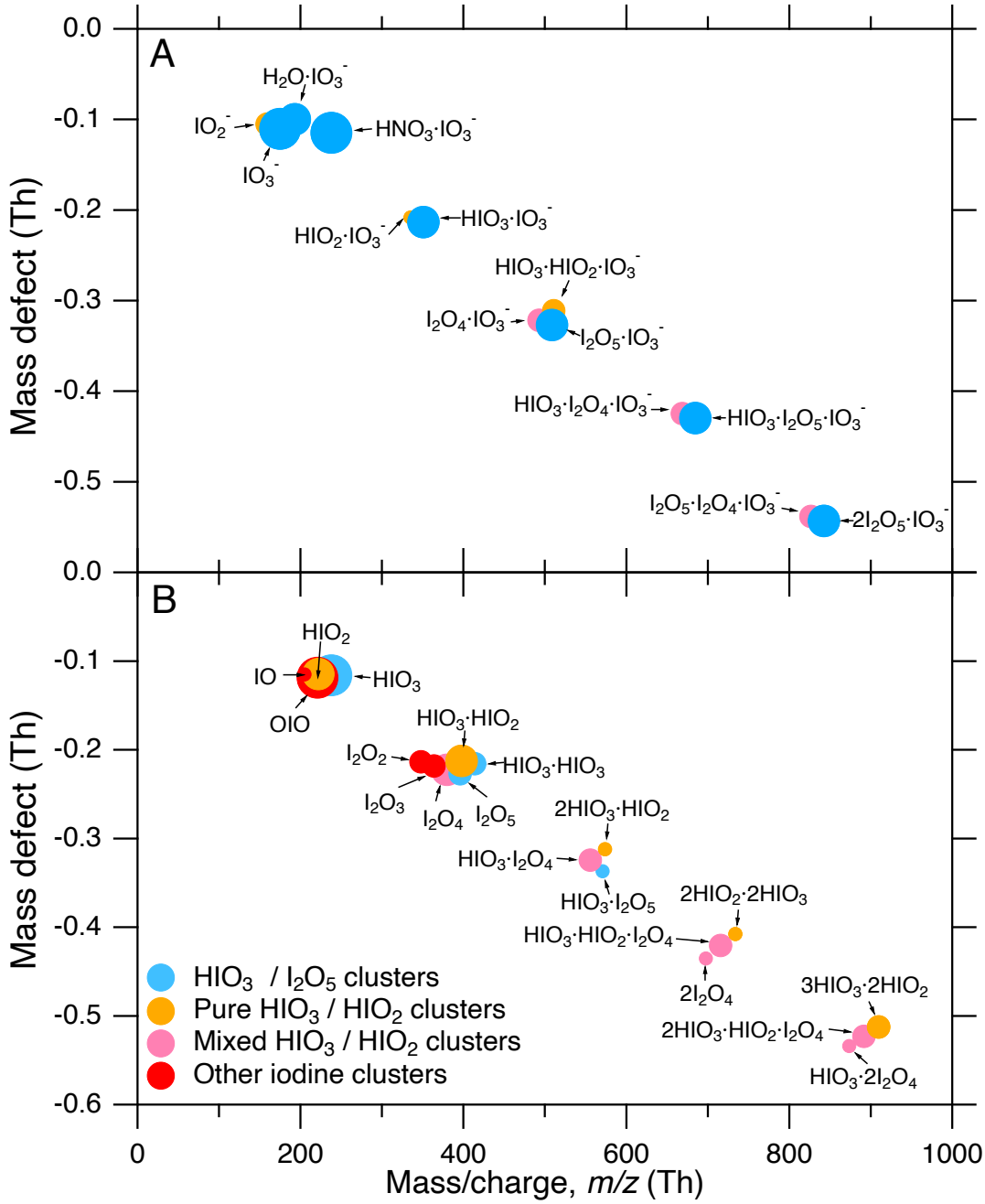

Fig. 2. Charged and neutral mass defect plots during nucleation events. Cluster mass defect (difference from integer mass) versus *m/z* of A) negatively charged and B) neutral clusters containing up to five iodine atoms during nucleation events. The experimental conditions are A) 36 ppbv O_3, 40% RH, +10 °C, 168 pptv I_2 and 1.5×10^7 I atom $cm^{-3}s^{-1}$ and B) 46 ppbv O_3, 43% RH, +10 °C, 49 pptv I_2 and 2.4×10^5 I atom $cm^{-3}s^{-1}$. The event shown in panel A) is continued in Fig. S3 up to clusters containing twelve iodine atoms. In order to simplify panel B), water molecules and nitrate charger ions are ignored (Fig. S4 shows the same event where they are included). Charged clusters are measured with the APiTOF(-) and neutral clusters with the nitrate-CIMS

(preceded by an ion filter). We find no nucleation takes place for positively charged clusters (Figs. S5 and S6). Blue circles indicate clusters containing only HIO_3 and I_2O_5. Orange circles indicate clusters containing only HIO_3 and HIO_2. Pink circles indicate clusters containing HIO_3, HIO_2, I_2O_5 and I_2O_4. Red circles indicate other iodine-containing neutral clusters. The area of the circle indicates signal strength on a logarithmic scale. Further details of the clusters and their signal strengths are provided in Table S2.

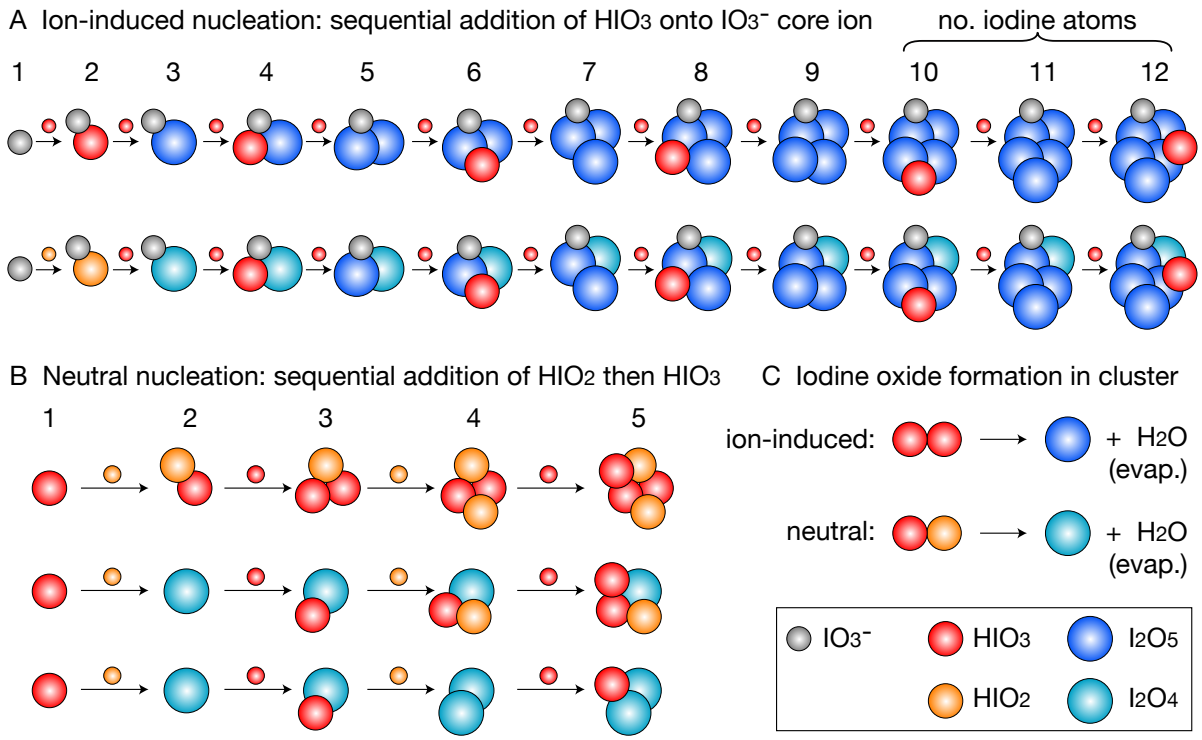

Fig. 3. Nucleation mechanisms for iodine oxoacid clusters. Schematic representations of the nucleation mechanisms for A) ion-induced (charged) and B) neutral (uncharged) iodine oxoacid clusters, interpreted from the mass defect plots. Ion-induced nucleation involves condensation of iodic acid (HIO_3) alone onto an IO_3^- ion, whereas neutral nucleation involves repeated stepwise condensation of iodous acid (HIO_2) followed by iodic acid. Iodine oxide formation takes place in the clusters, as shown in panel C). Pairs of HIO_3 molecules always dehydrate to form I_2O_5 in charged clusters (panel A). However, HIO_3 molecules do not form I_2O_5 in neutral clusters but some may combine with HIO_2 and dehydrate to form I_2O_4 (panel b). The relative intensities of the final neutral clusters in panel b) are $(HIO_3)_3 \cdot (HIO_2)_2$: $(HIO_3)_2 \cdot HIO_2 \cdot I_2O_4$: $HIO_3 \cdot (I_2O_4)_2$ = 0.38 : 0.46 : 0.16, indicating that the formation rate of I_2O_4 in the neutral clusters is comparable to the monomer collision rate.

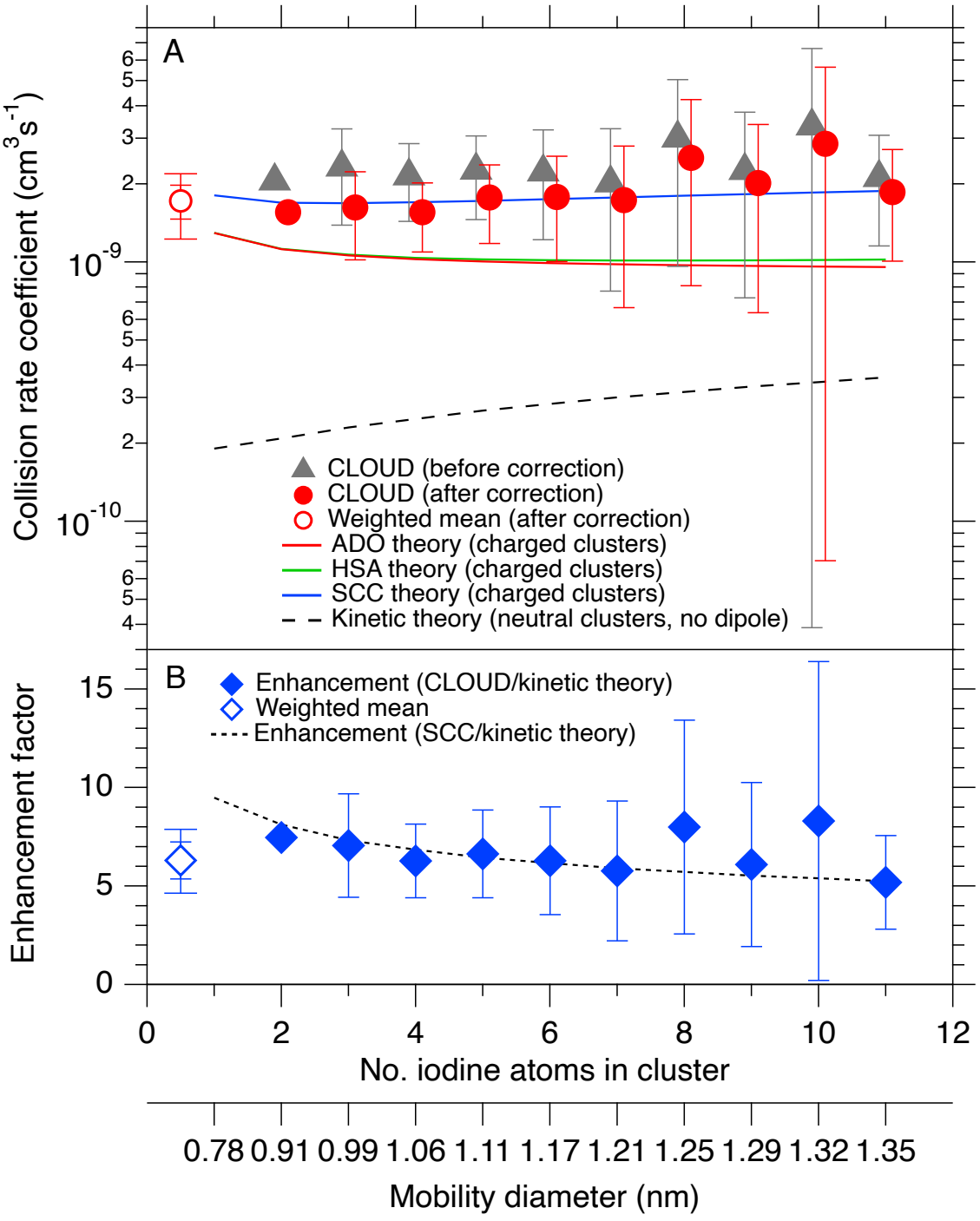

Fig. 4. Collision rate coefficients for ion-induced iodic acid nucleation. A) Collision rate (reaction rate) coefficients measured between neutral HIO_3 monomers and charged clusters containing up to 11 iodine atoms. The experimental conditions are 20-41 ppbv O_3, 34-44% RH, +10 °C, 0.4-3.5 pptv I_2 and (0.44-3.2)×10^5 I atom cm^{-3}s^{-1}. The grey triangles are calculated from the 50% appearance times of a total of 8 experiments with (0.76-2.0)×10^7 cm^{-3} HIO_3. The red

circles are the final experimental values after applying corrections from a kinetic model. The experimental points are horizontally shifted from integers to avoid overlaps. The solid curves show theoretical expectations for the charged collision rate coefficients from average dipole orientation theory (ADO, red curve (*36*)), hard-sphere average dipole orientation theory (HSA, green curve (*37*)) and surface charged capture theory (SCC, blue curve (*37*)). The expected collision rate coefficients between neutral monomers and neutral clusters, ignoring dipole-dipole interactions, are shown by the dashed black curve. Panel B) shows the measured enhancement factors for charged versus neutral collision rate coefficients (ratios of the corrected CLOUD measurements divided by the neutral collision rate coefficients). The black dotted line is the ratio of the SCC value to the neutral kinetic theory value. For both panels, the hollow markers show the weighted mean values from the trimer to 11-mer, with $\pm 1\sigma$ errors indicating statistical without (inner caps) and with systematic errors (outer).

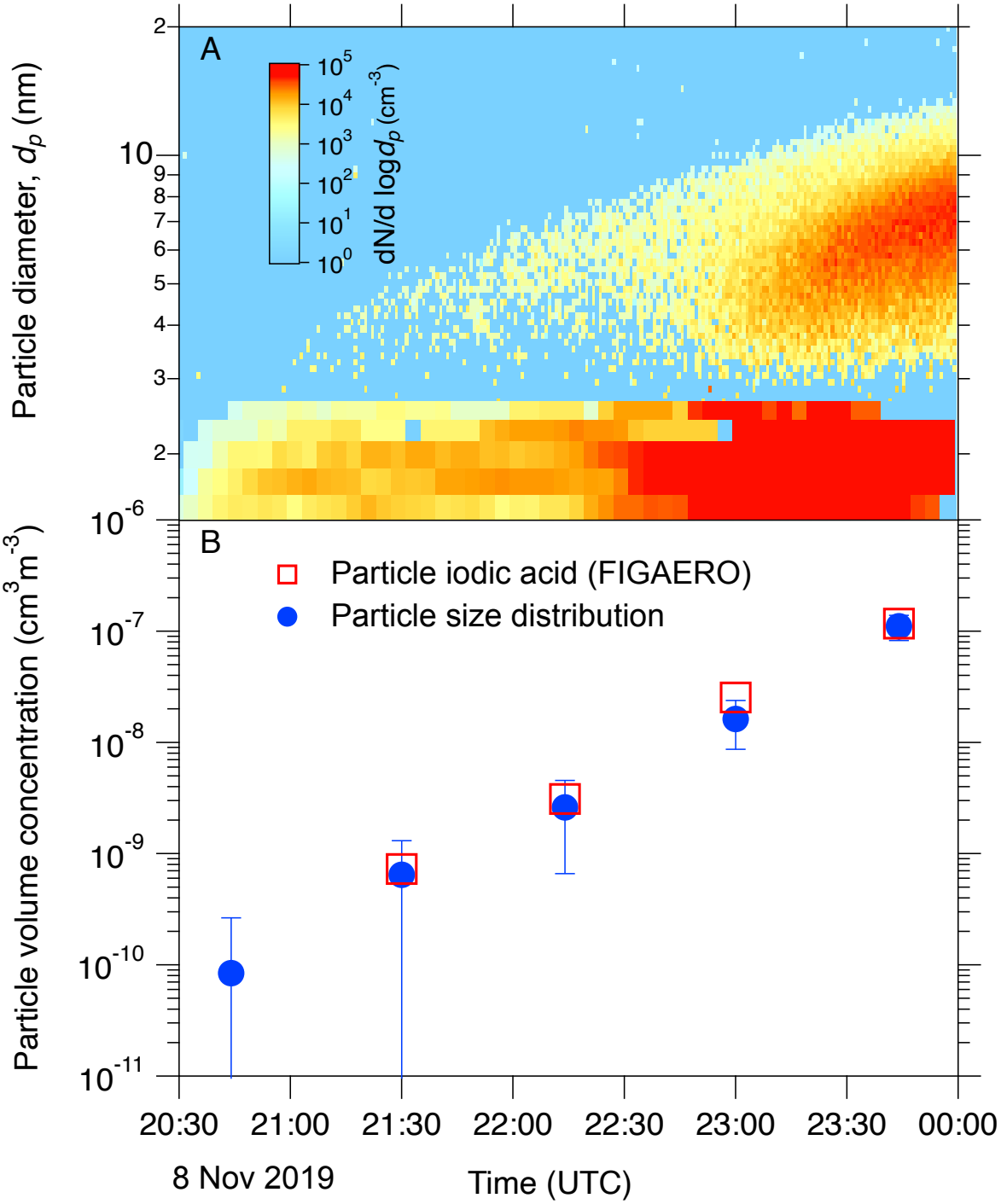

Fig. 5. Evolution of particle size and chemical composition during iodic oxoacids nucleation. A) Evolution of the particle size measured by the PSM (below 2.5 nm) and nano-SMPS (above around 4 nm). The experimental conditions are 40 ppbv O_3, 40% RH, +10 °C, 8 pptv I_2, (2.9-5.3)×10^5 I atom cm^{-3}s^{-1} and (3.1-7.1)×10^7 cm^{-3} HIO_3. The event is started by switching on green illumination (528 nm), and HIO_3 is increased towards the end. B) Evolution of the particle volume concentration derived from i) the particle size distribution (blue circles) and ii) the HIO_3 volume for particles collected and analyzed with the FIGAERO (hollow red squares). Particle

concentrations in the size range between 2.5 nm and 4 nm are obtained by interpolation between the PSM and nano-SMPS distributions and are verified by measurements of the total number concentrations above 2.5 nm threshold with the PSM. The FIGAERO collects particles on a Teflon filter for 30 min and then evaporates the sample with a controlled temperature ramp over the following 15 min at the inlet of the mass spectrometer. The FIGAERO data points are centered on the 30 min collection interval. The bars indicate ±1σ total errors. The FIGAERO mass spectrum shows that HIO_3 dominates the particle composition (80% mass fraction). This is independently confirmed by the close agreement between the volume concentrations measured by the particle sizers and by the FIGAERO (panel A).

Science
AAAS

Supplementary Materials for

Role of iodine oxoacids in atmospheric aerosol nucleation

Xu-Cheng He[1*], Yee Jun Tham[1], Lubna Dada[1], Mingyi Wang[2], Henning Finkenzeller[3], Dominik Stolzenburg[4,1], Siddharth Iyer[5], Mario Simon[6], Andreas Kürten[6], Jiali Shen[1], Birte Rörup[1], Matti Rissanen[5], Siegfried Schobesberger[7], Rima Baalbaki[1], Dongyu S. Wang[8], Theodore K. Koenig[3], Tuija Jokinen[1], Nina Sarnela[1], Lisa J. Beck[1], João Almeida[9], Stavros Amanatidis[10], António Amorim[11], Farnoush Ataei[12], Andrea Baccarini[8], Barbara Bertozzi[13], Federico Bianchi[1], Sophia Brilke[4], Lucía Caudillo[6], Dexian Chen[2], Randall Chiu[3], Biwu Chu[1], António Dias[11], Aijun Ding[14,34], Josef Dommen[8], Jonathan Duplissy[1,15], Imad El Haddad[8], Loïc Gonzalez Carracedo[4], Manuel Granzin[6], Armin Hansel[16,26], Martin Heinritzi[6], Victoria Hofbauer[2], Heikki Junninen[17,1], Juha Kangasluoma[1], Deniz Kemppainen[1], Changhyuk Kim[10,18], Weimeng Kong[10], Jordan E. Krechmer[19], Aleksander Kvashin[20], Totti Laitinen[1], Houssni Lamkaddam[8], Chuan Ping Lee[8], Katrianne Lehtipalo[1,21], Markus Leiminger[16,26], Zijun Li[7], Vladimir Makhmutov[20], Hanna E. Manninen[9], Guillaume Marie[6], Ruby Marten[8], Serge Mathot[9], Roy L. Mauldin[22], Bernhard Mentler[16], Ottmar Möhler[13], Tatjana Müller[6], Wei Nie[14,34], Antti Onnela[9], Tuukka Petäjä[1], Joschka Pfeifer[9], Maxim Philippov[20], Ananth Ranjithkumar[23], Alfonso Saiz-Lopez[24], Imre Salma[25], Wiebke Scholz[16,26], Simone Schuchmann[27], Benjamin Schulze[10], Gerhard Steiner[16], Yuri Stozhkov[20], Christian Tauber[4], António Tomé[28], Roseline C. Thakur[1], Olli Väisänen[7], Miguel Vazquez-Pufleau[4], Andrea C. Wagner[3,6], Yonghong Wang[1], Stefan K. Weber[9], Paul M. Winkler[4], Yusheng Wu[1], Mao Xiao[8], Chao Yan[1], Qing Ye[2], Arttu Ylisirniö[7], Marcel Zauner-Wieczorek[6], Qiaozhi Zha[1], Putian Zhou[1], Richard C. Flagan[10], Joachim Curtius[6], Urs Baltensperger[8], Markku Kulmala[1,14,15,29], Veli-Matti Kerminen[1], Theo Kurtén[30], Neil M. Donahue[2,31,32,33], Rainer Volkamer[3], Jasper Kirkby[9,6*], Douglas R. Worsnop[1,19], Mikko Sipilä[1*]

Corresponding authors. Email: xucheng.he@helsinki.fi (X.-C.H.), jasper.kirkby@cern.ch (J.Ki) and mikko.sipila@helsinki.fi (M.Sip.)

This PDF file includes:

1 Materials and Methods

The CLOUD experiment. The experiments described in this study are conducted at the CLOUD atmospheric simulation chamber (Cosmics Leaving Outdoor Droplets) at CERN (European Centre for Nuclear Research), Geneva, Switzerland. The chamber has been described in detail elsewhere (e.g., Kirkby *et al.* (*6*) and Duplissy *et al.* (*39*)). The volume of the stainless-steel chamber is 26.1m^3. Ultra-pure synthetic air derived from cryogenic liquids (21% oxygen, 79% nitrogen) is continuously flowed into the chamber at 250-300 standard litre per minute (slpm). Magnetically-driven mixing fans at the top and bottom of the chamber establish near-homogeneous conditions within several minutes. The experiments are conducted under very clean conditions, with total light organics contamination below 150 pptv (*6*).

The synthetic air injected into the chamber is humidified with ultra-purified water. Ozone is generated in dry synthetic air under UV irradiation, and added to the main substitution flow. The injection of gaseous iodine into the chamber is provided from crystalline iodine (I_2, Sigma-Aldrich, 99.999% purity) in a temperature-controlled evaporator to achieve levels of 0.4 to 168 pptv in the chamber. The injection lines are temperature stabilized and sulfinert-coated to minimize line conditioning effects. Trace gases are injected at the bottom of the chamber and dispersed in the chamber by the bottom fan.

The CLOUD chamber has unique control of ion concentrations. Electrodes installed in the chamber produce a 20 kV m^{-1} electric field to sweep out ions in under 1 second (neutral conditions), so ions do not influence new particle formation or growth rates. When the electric clearing field is off, ions are produced by galactic cosmic rays (gcr conditions), allowing study of new particle formation under typical sea level ion concentrations. Additionally, irradiation of the chamber with the pion beam allows experiments at ion concentrations typical of the tropopause (beam conditions).

Instrumentation. A key factor limiting our understanding of iodine oxidation and new particle formation has so far been our inability to measure most of the gas-phase iodine species, as well as the difficulty of carrying out online-measurements of the composition of nucleation mode particles. In this study, we deployed a series of mass spectrometers to measure simultaneously the charged, neutral and particle phase iodine species. Among these instruments, a bromide chemical ionization atmospheric pressure interface time-of-flight mass spectrometer (bromide-CIMS) provides a high-sensitivity measurement of I_2, and adapted Filter Inlet for Gases and AEROsols (FIGAERO)-CIMS (*40*) using bromide anions identifies the composition of nucleation mode particles.

APi-TOF(+/−). Atmospheric Pressure interface Time-Of-Flight mass spectrometers (APi-TOF, Aerodyne Inc.) are used to measure clusters charged by galactic cosmic rays or pions from the CERN beam (*41*). We deployed two APi-TOFs, one operating in positive mode and one in negative mode.

Nitrate-CIMS. The nitrate-CI-APi-TOF (nitrate-CIMS) is an APi-TOF coupled with a chemical ionization unit using nitric acid as the reagent gas. It is used extensively for detecting sulfuric acid, highly oxygenated organic molecules and iodic acid (HIO_3). The instrument was originally described by Jokinen *et al*. (*42*), whereas details of the instrument used in the present study can be found in Kürten *et al*. (*43*). The nitrate-CIMS has an ion filter integrated in its sampling line in order to avoid confusion with ions and charged clusters from the CLOUD chamber; thus, it measures only neutral molecules and clusters in CLOUD.

Bromide-CIMS. The bromide-CI-APi-TOF (bromide-CIMS) is an APi-TOF coupled with a chemical ionization unit using dibromomethane (CH_2Br_2) as the reagent gas. The CH_2Br_2 is fed into the sheath flow of the inlet, under the illumination of a soft X-ray source, producing bromide anions (Br^-). The Br^- ions are directed into the sample flow by a negative electric field, which then cluster with neutral molecules in the sample air. The bromide-CIMS in this study is mainly used to measure molecular iodine (I_2), which is the precursor to produce I_xO_y and iodine oxoacids.

CE-DOAS. Gaseous molecular iodine concentrations are precisely measured with closed-path Cavity Enhanced Differential Optical Absorption Spectroscopy (CE-DOAS), using a green LED, high reflectivity mirrors (Advanced Thin Films), and a Czerny-Turner spectrometer with 0.5 nm optical resolution (Acton SP2150). The I_2 limit of detection is 25 pptv for 1 min integration time, and 8 pptv for 10 min integration time. The optical path length in the instrument is around 20 km, determined by comparison of LED intensities in nitrogen and helium (*44*, *45*). The accuracy for the CE-DOAS iodine time trace is estimated to be 20%, as a combination of cross section uncertainty and fit sensitivities. I_2 concentrations are generally well below 10 pptv in most of the experiments but reach up to 1.7 ppbv during selected experiments for calibration purposes. Thereby, the CE-DOAS is used to calibrate the bromide-CIMS, which provides precise I_2 concentrations at lower concentrations used in this study. A tight near-linear correlation to the bromide-CIMS time series is found and approximated by a quadratic fit. The calibration of the bromide-CIMS is estimated to be better than 30%.

Light source. We used a green light to photolyze I_2 and to drive the iodine chemistry and subsequent new particle formation. The actinic fluxes for photolytic conversion of molecular iodine into iodine atoms are driven by an array of 48 green LEDs (light sabre 4, LS4), protruding into the chamber in the mid plane. The maximum total optical power output is 153W, centered on 528 nm. This corresponds to a maximum iodine photolysis rate $j = 7\times10^{-3}$ s^{-1} and an I_2 lifetime of 2.4 min. The photolysis rate is calculated from the decay rate of I_2 at a fixed light intensity. Actinic fluxes are regulated by controlling the number of LEDs used and the set point of individual LED. Light fluxes are monitored by two photodiodes and a spectrometer. Finally, we calculate the iodine atom production rate by doubling the multiple of I_2 concentration and iodine photolysis rate. Due to the high uncertainty in scaling the light fluxes to photolysis rates, we expect an overall a factor of three uncertainty in iodine atom production rate estimation.

FIGAERO(Br^-)-CIMS. The FIGAERO(I^-)-CIMS (*40*) is a widely used method to measure organic and inorganic aerosol composition. FIGAERO is a manifold inlet for APi-TOF with two operating modes. In one mode, gases are directly sampled into a turbulent flow ion-molecule reactor while nucleated particles are concurrently collected on a PTFE (polytetrafluoroethylene) filter via a separate dedicated port. In the other mode, the filter is automatically moved into a pure

N_2 gas stream flowing into the ion molecule reactor while the N_2 is heated to evaporate the particles via temperature-programmed desorption. However, the use of iodide (I^-) as the reagent ion would prevent it from being used to measure the composition of iodine-containing particles. Therefore, the FIGAERO used in this study uses CH_2Br_2 as the reagent gas, since Br^- has a high affinity for iodine-containing molecules. This is the first reported operation of a Br^--FIGAERO, which provides critical insight into the composition of iodine particles. The gas and particle phase sampling rates are 18 and 6 slpm, respectively. The particle collection period lasts 30 minutes and the detection limit of particulate HIO_3 is 3 ng m^{-3}.

Particle-phase HIO_3 is quantified by a series of laboratory calibration experiments that collect suspended HIO_3 particles onto the FIGAERO filter over several time intervals (0, 15, 30 and 60 minutes) and analyze them with the same FIGAERO procedure as used at CLOUD. HIO_3 particles were constantly generated by nebulizing HIO_3 (≥ 99.5%, Sigma-Aldrich) water solution with an atomizer (TOPAS ATM 221), dried with a home-made diffusion dryer, and characterized with a TSI nano-SMPS. The generated particles have a geometric mean diameter of 14 nm and a total number concentration of 6.0×10^3 cm^{-3}, comparable to those during the new particle formation experiments in CLOUD. To calculate the particle volume from HIO_3, we assume the bulk density of HIO_3 (4.62 g cm^{-3}). The log-scale slope between collected particle volume and particulate HIO_3 signal is better than 0.96. We note that, after going through the diffusion dryer, HIO_3 particles might not be completely effloresced, and so residual water content in the particles may cause a slight overestimate of the particle volume derived from FIGAERO particulate HIO_3 in Fig. 5B.

PSM. A scanning particle size magnifier (*46*) (PSM, Airmodus Ltd.) coupled to a condensation particle counter (CPC) is used to detect particles with a detection threshold between 1 and 3 nm. The PSM uses diethylene glycol as a working fluid to grow the particles before counting them by the CPC. The PSM is used to determine the nucleation rate at 1.7 nm ($J_{1.7}$) and the number size distribution of particles between 1–3 nm.

NAIS. A Neutral cluster and Air Ion Spectrometer (NAIS) measures the mobilities and concentrations of the negative and positive clusters (*47*).

DMA-train. A differential mobility analyzer train (*48*) (DMA-train) measures the particle growth rates between 1.8 – 3.2 nm with high precision and sampling rate.

Nano-SMPS. A nano-scanning mobility particle sizer (nano-SMPS (*49*), TSI-3938) measures the particle size distribution between 4 and 65 nm. Particle concentrations in the size range between 2.5 and 4 nm are obtained by subtracting the total particle concentration above 4.0 nm measured by the nano-SMPS from the total particle concentration above 2.5 measured by the PSM. Particles between 2.5 nm and 4 nm are all considered 4 nm in the calculation of particle volume concentration in Fig. 5B, and it contributes less than 10% in the total volume concentration.

Nucleation rates. The nucleation rates of particles with diameter 1.7 nm and above are calculated using the same method as described in Dada *et al.* (*50*). Briefly, they are calculated according to the balance equation:

$$J = \frac{\mathrm{d}N}{\mathrm{d}t} + S_{dil} + S_{wall} + S_{coag}\ (\mathrm{cm^{-3}s^{-1}})$$

where N is the particle number concentration above 1.7 nm; S_{dil}, S_{wall} and S_{coag} are dilution, wall loss and coagulation losses, respectively. Typical values for S_{dil} and S_{wall} are 1.6×10^{-4} s^{-1} and 2.2×10^{-3} s^{-1}, respectively, while S_{coag} depends on the number and size distribution of particles in the chamber.

Growth rates. The particle growth rates are calculated by the 50% appearance time method as described in Lehtipalo *et al*. (*51*). Growth rates between 1.8–3.2 nm are calculated from the DMA-train.

Quantum chemical calculations. The initial conformer sampling of monomers was carried out in the Spartan 18 program using the MMFF force field (though most monomers in this study only had one conformer). Partial charges of different atoms in the monomers were then computed at the ωB97X-D/aug-cc-pVTZ-PP level of theory by running a single-point calculation with the Pop=MKUFF keyword using the Gaussian 09/16 program (*52*). The monomer geometries and partial charges were then used by the ABCluster (*53*, *54*) program to generate the initial structures for the dimer cluster. 200 initial structures were generated and the best 100 out of them were selected after the ABCluster procedure. During the ABCluster procedure, configurational sampling of the dimer clusters was performed using molecular mechanics (keeping the monomer structures rigid), with the intermolecular interactions defined by the CHARMM force field and the computed partial charges (*55*). Single point XTB calculations were further used to reduce the number of conformers for further analysis. Conformers within 7 kcal mol^{-1} in relative electronic energy compared to the lowest-energy conformer were selected for further analysis. The initial monomer and cluster sampling, as well as the XTB energy calculations, used iodine atoms. However, the iodine atoms in the generated clusters were subsequently replaced by bromine, and the obtained clusters were optimized at the B3LYP/6-31+G* level using Gaussian. The replacement of iodine by bromine was done because the (computationally very efficient) 6-31+G* basis set has not been defined for iodine atoms. However, extensive test calculations (*56*) demonstrate that the geometries of I and Br-containing clusters are very similar. Optimized conformers within 6 kcal mol^{-1} in relative electronic energy compared to the lowest-energy conformer were then selected for further calculations, and bromine atoms were again replaced back to iodine atoms. The structures were then re-optimized, and vibrational frequencies calculated, at the ωB97xD//aug-cc-pVTZ-PP (*57*, *58*) level. Iodine pseudopotential definitions were taken from the EMSL basis set library (*57*). Similar procedures have been utilized in Hyttinen *et al*. (*56*). An additional coupled-cluster single-point energy correction was performed on the lowest-energy conformer calculated at the ωB97xD//aug-cc-pVTZ-PP level. The coupled cluster calculation was performed using the DLPNO-CCSD(T)/def2-QZVPP method with the ORCA program ver. 4.1.1 (*59*, *60*). The polarizability and dipole moment of HIO_3 were also calculated at the ωB97X-D/aug-cc-pVTZ-PP level.

Kinetic model. The calculated new particle formation rates at +10°C for the ion-induced case (HIO_3 model, J_{iin}) in Fig. 1A are based on the numeric model presented by Kürten *et al*. (*61*) and Kürten (*62*). Despite the model was originally constructed to calculate neutral new particle formation rates, we adopted identical parameterizations presented in He *et al.* (*32*) and modified the model to simulate ion-induced iodic acid nucleation. It is shown in this study (figs. S3, S5 and

S6) and He *et al.* (*32*) that only negatively charged ion clusters grow and that this growth is mainly due the addition of neutral HIO_3 molecules. Therefore, positively charged clusters are parameterized as sinks for negatively charged clusters. Additionally, since neutral clusters are shown to have a limited contribution to the ion-induced iodic acid nucleation (*32*), they are not considered in our simulations (contribution of neutral nucleation is not included in the simulations). In this way, we can clearly separate the contribution of ion-induced nucleation and neutral nucleation at the given experimental conditions. These assumptions lead to the following formulation of differential equations that are solved by the model. The balance equation for the positively charged monomer concentration (N_1^+) is:

$$\frac{dN_1^+}{dt} = q - \left(k_{w,1} + k_{dil} + k_{rec} \cdot \sum_{i=1}^{n} N_i^-\right) \cdot N_1^+$$

where $k_{w,1}$ is the wall loss rate for monomers, k_{dil} is the chamber dilution loss rate and k_{rec} is the recombination rate (2.2×10^{-6} cm^3 s^{-1}). The ion pair production rate, q, is taken as 4.1 cm^{-3} s^{-1}. The negatively charged monomer concentration (N_1^-, i.e., IO_3^-) can be described by:

$$\frac{dN_1^-}{dt} = q - \left(k_{w,1} + k_{dil} + k_{rec} \cdot N_1^+ + k_{1,1} \cdot N_1^0\right) \cdot N_1^-$$

Here, it is important to note that the ion can grow due to the collision with a neutral acid molecule (N_1^0, i.e., HIO_3). The ion-neutral collision rate coefficient, $k_{1,1}$, for the present chemical system is 1.7×10^{-9} cm^3 s^{-1}. The negatively charged cluster ion concentrations for $i \geq 2$ (N_i^-, where $i = 2$ corresponds to a negatively charged dimer) can be calculated according to:

$$\frac{dN_i^-}{dt} = k_{i-1,1} \cdot N_{i-1}^- \cdot N_1^0 - \left(k_{w,i} + k_{dil} + k_{rec} \cdot N_1^+ + k_{i,1} \cdot N_1^0\right) \cdot N_i^-$$

As the charged clusters grow at the kinetic limit, no evaporation rates are taken into account (*32*). Finally, the new particle formation rate for the ion-induced case, J_{iin}, is taken as the production term at the critical cluster size of 1.7 nm:

$$J_{iin} = k_{n_{crit}-1,1} \cdot N_{n_{crit}-1}^- \cdot N_1^0$$

In the model a fixed monomer acid concentration (N_1^0) is used and the J_{iin} is taken as the steady-state value. The same ion-neutral collision rate coefficient (1.7×10^{-9} cm^3 s^{-1}, see above) is used for all cluster sizes as the rate coefficient is not expected to change significantly for charged clusters below 1.7 nm (e.g., Fig. 4 shows the rate coefficients of dimer to 11-mer). A value of 4.62 g cm^{-3} for the density (bulk density of iodic acid) and 176 g mol^{-1} for the molecular weight are used for HIO_3 as the lower end of the simulation in Fig. 1A. Additionally, as Khanniche *et al.* (*63*) concluded that the dihydrates of HIO_3 are stable below 310 K, we include a simulation with a value of 2.86 g cm^{-3} for the density and 212 g mol^{-1} for the molecular weight for HIO_3 + two water molecules ($HIO_3 \cdot 2H_2O$) as the higher end of the simulation in Fig. 1A. The addition of water molecules increases the contributed volume of HIO_3 monomer which in turn reduces the amount of HIO_3 monomers needed to reach the critical cluster size of 1.7 nm. The simulation (red band in Fig. 1A) agrees well with our measured J_{gcr} within measurement uncertainties, below HIO_3 of 2×10^7 cm^{-3}, where J_n is negligible.

2 Collision rate coefficients

2.1 Calculation of collision rate coefficient from theoretical methods

There are three theoretical methods which are compared with our measurement data: the widely-used "average dipole orientation theory" (ADO theory) (*33*), the hard-sphere average dipole orientation theory (HSA theory), and the surface charge capture theory (SCC theory) (*34*). These methods are detailed in the original literature, and we only briefly compare them here. The ADO theory considers the thermal rotational energy of polar molecules, but it treats the charged cluster as a single point. The HSA theory extends the ADO theory by including the physical size of the charged cluster in the derivation, which in turn increases the predicted collision rate coefficients. This is particularly important for large charged clusters, while it has only a small effect for the charged clusters in this study (<1.5 nm). Finally, the SCC theory assumes that the charge can freely move around the cluster. When collision occurs, the charge tends to move to the nearby surface of the cluster, which increases the effective capture radius and hence also the collision rate coefficient.

2.2 Calculation of apparent collision rate coefficient from measurement data

Detailed derivation of the appearance time method which we apply to the calculation of collision rate coefficients can be found in He *et al.* (*32*). Briefly, an APi-TOF operating in negative ion mode was deployed to measure the sequential growth of charged molecular clusters in ion-induced iodic acid nucleation experiments. The 50% appearance time method [APP50, (*51*)] was then applied to the time evolution of the charged clusters to obtain appearance times. The apparent collision rate coefficient between the (i+1)-mer cluster and HIO_3 molecules is calculated according to

$$k_{i+1} = \frac{1}{[HIO_3]_{\text{avg}} \times (t_{i+1,50} - t_{i,50})}$$

where $t_{i+1,50}$, $t_{i,50}$ are the 50% appearance times of the (i+1)-mer and i-mer, respectively, and $[HIO_3]_{\text{avg}}$ is the averaged HIO_3 concentration during the time interval [$t_{i+1,50}$, $t_{i,50}$]. The results are shown in Fig. 4A as "CLOUD, before correction". These values are also inferred as "apparent collision rate coefficients".

2.3 Correction of the apparent collision rate coefficient

However, as detailed in He *et al.* (*32*), the deviation of the APP50 method neglected a number of processes that affect the ion distributions. These processes include ones that directly affect the full cluster population (coagulation, wall losses, dilution and evaporations), ones that only affect charged clusters (ion production in the chamber and ion-ion recombination), and the finite time resolution of the measurements of both physical and chemical properties. The Polar ANd high-altituDe Atmospheric research 520 (PANDA520) model was originally developed in He *et al.* (*32*) to simulate charged iodic acid cluster formation processes. In this study, we further develop a method to correct the apparent collision rate coefficient for the neglected processes.

In order to run the model, the collision rate coefficient based on surface charge capture (SCC) theory was input into the model. This is because the SCC theory produced the closest results to the apparent collision rate coefficient as shown in Fig. 4A. Then, the charged cluster distributions from the model output data were used to calculate the apparent collision rate coefficient based on the APP50 method. The apparent collision rate coefficient was then compared with the SCC theory values. Correction factors are thus derived for individual charged clusters as the ratio of the SCC predicted values to calculated apparent collision rate coefficients. The final measured collision rate coefficients are obtained by applying the correction factors to the apparent collision rate coefficients.

However, it needs to be noted that there are two sets of correction factors, since our experiments can either start from ion-free conditions or from ion-present conditions. First and the most common way to start an experiment was to switch on the green light to photolyze molecular iodine. This approach produces charged clusters and HIO_3 from clean conditions. Some initial IO_3^- anions may be present owing to a low residual level of HIO_3 that is almost always present in the chamber at the beginning of the experiments. Although the residual concentration is too low to grow charged clusters, it is sufficient to produce IO_3^- anions since HIO_3 is a strong acid and thus an efficient proton donor. The residual IO_3^- can confound estimation of the appearance time for IO_3^-, and thereby, affect the estimation of the collision rate coefficient of $HIO_3 \cdot IO_3^-$ with HIO_3. There were six experiments belong to this group.

The second way was to start an experiment from ion-free conditions. By turning the electric fields off, primary ions produced by gcr could survive and grow. The green light was always turned on to maintain a stable production of HIO_3. There were two experiments belong to this group. Only runs with the second method were used to calculate the collision rate coefficient of the dimer (k_2). Due to this lack of statistics in the estimation of k_2, we do not determine a corresponding error bar.

We applied the correction factors produced by the PANDA520 model (on average 0.79) to the apparent collision rate coefficients derived from the measurements (denoted "CLOUD, before correction" in Fig. 4A) to calculate the final collision rate coefficient ("CLOUD, after correction"). Additionally, in order to rule out that the correction factors are sensitive to initial input values, we replaced the values calculated by the SCC theory with values from the ADO theory in the model. This yielded an average correction factor of 0.75–very close to the value obtained using the SCC rate coefficients as input. Thus, the values of the correction factors obtained indeed depend mainly on the loss processes, and not on the absolute values of the input collision rate coefficients (as long as reasonable values are used).

3 Measurement sites

3.1 Hyytiälä

The SMEAR II (Station for Measuring Ecosystem-Atmosphere Relations) is a measurement station located in Southern Finland, 220 km northwest from Helsinki and about 60 km northeast from Tampere (61° 51′ N, 24° 17′ E). The measurement station is in a rural continental site surrounded by mostly Scots-pine forests (*64*).

3.2 Aboa

The Finnish Antarctic research station (Aboa) is located on Basen Nunatak at Vestfjella mountains in Queen Maud Land, Eastern Antarctica (73° 03′ S, 13° 25′ W). The measurement site is 480 m above sea level and 130 km south of the edge of sea ice (*35*).

3.3 Ny Ålesund

The Gruvebadet Observatory is located at about 50 m above sea level, 800 m southwest from the Ny-Ålesund village Svalbard (78° 55′ N, 11° 56′ E).

3.4 Greenland

Villum Research Station, Station Nord, is located in the northeastern corner of Greenland (81° 36′ N, 16° 40′ W). It is on Prinsesse Ingeborg Halvø peninsula.

3.5 Beijing

The Beijing site is located in the west campus of Beijing University of Chemical Technology (39° 94′ N, 116° 30′ E) (*65*). The campus is surrounded by commercial properties and residential buildings. Thereby, the station represents a typical urban site.

3.6 Helsinki

The SMEAR III station is an urban measurement site located in the Kumpula campus, University of Helsinki (60° 12′ N, 24° 58′ E). It is about 4 km north-east from Helsinki city center (a coastal city), and on top of a hill (25 m above the sea level).

3.7 Mace Head

The Mace Head Research Station is located in Connemara, County Galway, Western Ireland, on the coast of Atlantic Ocean (53° 19′ N, 9° 53′ W) with regular tidal activity (*10*). The station is situated about 100 m from the shoreline.

3.8 Nanjing

The Nanjing measurement station, Station for Observing Regional Processes of the Earth System, Nanjing University (SORPES-NJU), is located about 20 km northeast of Nanjing, Eastern China (32° 07′ N, 118° 57′ E).

3.9 Réunion

Réunion Island (21.2 °S, 55.7 °E) is a volcanic island located in the southwestern part of the Indian Ocean. The measurement site was Maïdo-OPAR observatory (L'observatoire de physique de l'atmosphère de La Réunion), which is a modern research station located on top of an old volcanic caldera at 2160 m above the sea level. Maïdo-OPAR receives free tropospheric air masses during

the night-time and offers unique views on the southern hemispheric air masses. The station is part of many international research networks, e.g., GAW and ACTRIS, and hosts many permanent measurements on atmospheric composition.

3.10 Neumayer

The German Antarctica research station, Neumayer, is located on the Ekström ice shelf. The location of the site in 2016 was at 70° 40′ N, 8° 16′ E.

4 Implication of iodine oxoacid particle formation in the atmosphere

4.1 Pristine boundary layer

We are now able to assess with more confidence the global significance of iodine oxoacid particle formation. In coastal locations where active emissions occur (e.g., in Mace Head (*10*, *11*)), iodine-containing species can contribute significantly to new particle formation and growth to cloud condensation nuclei size; both charged and neutral cluster formation processes can dominate the overall cluster formation processes depending on the HIO_3 concentration. In polar regions, we observed significant geographical and temporal differences. At Aboa, HIO_3 levels were modest and thus we expect that HIO_3 has a minor role in new particle formation. At Villum station, neutral clusters formation dominated the iodine cluster formation processes because of the low temperature, while at Ny Ålesund and Neumayer III, both charged and neutral clusters potentially contributed to the cluster formation processes due to the relatively low temperature and moderate HIO_3 concentration (fig S9). Although HIO_3 was detected at Hyytiälä (boreal forest) and Réunion (at high altitude), the concentrations measured so far were too low for significant new particle formation.

4.2 Polluted boundary layer

Iodine particle formation is generally considered irrelevant for polluted urban environments. However, a feature of particular interest in our measurements is that we have measured noticeable HIO_3 in all of the three city sites for the first time (Helsinki, Finland; Beijing and Nanjing, China). In Nanjing (an inland city, roughly 300 km from the coast), the HIO_3 concentration was around 10^5 cm^{-3} for most of the time, but occasionally approaching 10^6 cm^{-3} (representing a growth rate of roughly 0.2 nm h^{-1}, at +10°C) in the measurement period. This suggests that HIO_3 has a little contribution to the particle formation processes in Nanjing most of the time. In Beijing, the daily peak concentrations of HIO_3 were above 10^6 cm^{-3} for almost the entire measurement period, and they were very often higher than 2×10^6 cm^{-3}. This suggests that HIO_3 could contribute at maximum 0.4 nm h^{-1} in the initial growth of newly formed particles in Beijing (figs. S9, S10). The seemingly small number cannot be ignored, since the typical particle growth rates in Beijing in was between 1 – 3 nm h^{-1} in August 2018 (*66*). Stolzenburg *et al.* concluded that the evaporation of sulfuric acid from particles above 2 nm is negligible and growth proceeds kinetically even with low ammonia concentration at temperatures between +5 to +20°C (*30*). Considering that HIO_3 is much less volatile than H_2SO_4, the same conclusion could also apply. Thereby, our results hint that HIO_3 could contribute to, despite not dominate, the initial growth of particles in Beijing in summer.

In Helsinki, we measured significant amount of HIO_3 in August 2019. The daily peak concentrations were often higher than 10^7 cm^{-3}, and occasionally even reaching 3×10^7 cm^{-3} at which ion-induced iodic acid nucleation starts to play a role. As shown in fig. S9, the approximate growth rates from HIO_3 were often above 1 nm h^{-1}, and reached 5 nm h^{-1} at maximum. Considering that a mean growth rate in August at Helsinki was around 6.5 nm h^{-1} (*67*), the contribution from HIO_3 in particle growth can be important at Helsinki in summer. Thereby, HIO_3 can contribute to both the nucleation and initial growth during summertime in Helsinki.

While it is relatively well-known that iodine particle formation is important in pristine coastal environments, its contribution to growth in an inland city (Beijing) and the contribution to both nucleation and growth in a coastal city (Helsinki) were not expected. Sive *et al.* found terrestrial sources of methyl iodide from vegetation and soils (*20*), despite iodine species had been widely considered marine originated. These sources may explain why we have measured HIO_3 ubiquitously at all the inland sites as shown in figs. S9 and S10.

4.3 Upper troposphere/low stratosphere

The widespread presence of iodine in the free troposphere has been reported repeatedly in the literature (*23–25*, *68*, *69*). Of particular note, iodine has been consistently observed in the vicinity of the tropopause (*24*, *68*, *70*, *71*), where temperatures are lowest and the strong temperature dependence of iodine oxoacid nucleation found in this study is likely to make it more relevant. The upper troposphere/lower stratosphere (UTLS) is also where galactic cosmic ray fluxes are at their maximum (*72*), further enhancing efficient ion-induced iodic acid nucleation, which is found to proceed at the kinetic limit already at/below +10 ℃. Additionally, large particles are sparse in the upper troposphere, decreasing the scavenging of condensable vapors such as HIO_3, as well as nano-clusters. All these conditions favor a potential contribution of iodine particle formation in these parts of atmosphere. New particle formation has been observed to be widespread in these regions over much of the world (*73*). The sharp conversion of gas-phase iodine to the particle phase, across the tropopause (*25*), consistent with the findings in this paper, suggests iodine likely participates in this widespread new particle formation. Indeed, particulate iodate (IO_3^-) is observed near the tropopause, and IO_3^- is the main reservoir of iodine in the stratosphere (*25*). The rapid nucleation and growth from iodine species help to carry aerosols through size ranges that are especially susceptible to scavenging by other aerosols or grow them to sizes where later growth from other condensable matter becomes effective. This is especially important in the UTLS, where changes to the radiative budget can impact large scale atmospheric dynamics (*74*, *75*). The observed threefold increase of surface iodine in recent decades (*37*, *76*, *77*) is expected to propagate to the UTLS (*25*) and therefore may exert a climate forcing via the nucleation mechanisms proposed in this study, among others.

The rather sparse observations of HIO_3 around the world reveal the need for more dedicated field measurements in order to elucidate the role of iodine particle formation at the surface and aloft. Combined with global simulations, these measurements can aid to identify the role of iodine particle formation in past, present and future climate systems.

5 The identity of the measured HIO_3 signals

Gaseous HIO_3 was first measured by Sipilä *et al.* in a coastal site in western Ireland (*11*). The measured gaseous HIO_3 signal comprises a few different peaks in the mass spectrum measured by the nitrate-CIMS, i.e., IO_3^-, $HIO_3 \cdot NO_3^-$, $HIO_3 \cdot HNO_3NO_3^-$ and a few hydrated forms of these charged clusters. The distribution of these anions depends mostly on the softness of the setting deployed by individual instruments. For example, a more fragmenting setting would increase the ratio of IO_3^- to $HIO_3 \cdot NO_3^-$ / $HIO_3 \cdot HNO_3NO_3^-$, and vice versa.

The authors have detailed several important experiments and discussed in the Supplementary Information on why the measured gaseous HIO_3 was indeed present in the atmosphere rather than artificially produced by the nitrate-CIMS (*11*). For instance, the authors injected a substantial amount of ammonia through the ion source of the nitrate-CIMS which activated the surface of the ion source preventing nitric acid from entering the ion-molecule reaction chamber. As expected, the observed nitrate anions (NO_3^-) almost dropped by an order of magnitude. However, the measured HIO_3 clusters increased compared to the control experiment in which the ammonia was not injected. This was the direct evidence that the measured HIO_3 clusters were not formed artificially from the nitrate anions by, for example,

$$NO_3^- + OIO \rightarrow IO_3^- + NO_2 \quad \text{(S1)}$$

since otherwise the concentration of the measured HIO_3 clusters would substantially decrease, rather than increase.

We further exclude this possibility in this study by deploying a nitrate-CIMS which was tuned to minimize the fragmentation in the ion optics of the instrument. We show a typical distribution of anions containing gaseous HIO_3 in table S2. As can be seen, the IO_3^- signal only consists less than 6% of the total HIO_3 signal, which in turn represents less than 6% of the reported gaseous HIO_3 concentration. Even if the reaction (S1) could occur, the influence on our gaseous HIO_3 measurements is still minor, not to say that this has already been proven not important in Sipilä *et al.* (*11*) at the first place.

Another important question that has not been confirmed is the identity of the measured gaseous HIO_3. HIO_3 has several isomers that can present in the atmosphere (*28*), and it has not been confirmed that the measured HIO_3 is iodic acid ($HOIO_2$). We confirm this by comparing the thermograms of the freshly formed small particles in the chamber and nebulized iodic acid – water solution in Fig. 5. As can be seen, the thermogram from the nebulized iodic acid–water solution shares identical features compared to the thermogram from freshly formed small particles in the chamber. This is a direct evidence that the measured HIO_3 signal is gaseous iodic acid, since if the identity of the HIO_3 signal is another isomer of iodic acid, the thermograms would not be identical.

6 Further remarks on the cluster formation mechanisms

Sipilä *et al.* (*11*) proposed that the general cluster formation mechanism for iodine-oxygen-hydrogen species in the atmosphere is

$$(HIO_3)_{0-1}(I_2O_5)_n + HIO_3 \rightarrow (HIO_3)_{1-2}(I_2O_5)_n \quad \text{(S2)}$$

$$(HIO_3)_2(I_2O_5)_n \rightarrow (I_2O_5)_{n+1} + H_2O \quad \text{(S3)}$$

where *n* is an integer. The proposed mechanism consists of two major reaction types: first, the collision between HIO_3 and iodine-containing clusters leads to cluster growth, and ultimately new particle formation. Additionally, the existence of two HIO_3 in a cluster would lead to a chemical process in which the two HIO_3 produce I_2O_5 and H_2O, as is shown in reaction (S3).

However, in the past years, several issues have arisen which shed doubt on this mechanism. First of all, Khanniche *et al*. (*78*) calculated the rate coefficient for the reaction of two HIO_3 forming one I_2O_5 and an H_2O, and reported it to be 5.56×10^{-24} cm^3 $molecule^{-1}$ s^{-1} at 300 K. This value, about 14 orders of magnitude below the gas-kinetic collision limit, would be far too slow to explain the fast cluster formation processes which have been observed in the atmosphere. Furthermore, their calculations indicate that the reverse reaction, in which an I_2O_5 and a H_2O form two HIO_3, is much more favorable, and has a rate coefficient of 1.03×10^{-22} cm^3 $molecule^{-1}$ s^{-1} at 300 K. Since the H_2O concentration is inevitably many orders of magnitude higher than the HIO_3 concentration, gas-phase formation of I_2O_5 from molecular HIO_3 would not be expected to be important in our atmosphere.

Second, Passananti *et al*. (*79*) recently concluded that the instrumental setting is crucial in determining the extent of collision-induced cluster fragmentation, which in turn affects the mass spectra we observe. In addition, the charging process itself (even in the absence of high energy collisions) may be sufficient to catalyze or induce chemical reactions which would not occur for neutral molecules or clusters. For these reasons, Sipilä *et al*. (*11*) could not exclude the possibility that the reaction (S3) could happen in the instrument itself, rather than in the atmosphere. An alternative pathway to form the observed charged clusters would be:

$$(HIO_3)_2(I_2O_5)_nE^- \rightarrow (I_2O_5)_{n+1}E^- + H_2O \quad \text{(S4)}$$

where E^- is a core anion. It is thus unclear whether the chemical reaction of two HIO_3 that leads to the formation of an I_2O_5 and an H_2O is a natural process which happens in neutral clusters, or instead, it happens in the measurement instrument, either due to the charging, or the collision-induced cluster fragmentation, or some combination of both.

To minimize the collision-induced cluster fragmentation, the nitrate-CIMS instrument deployed in this study was a soft-tuned instrument. However, it should be noted that due to the limitation of the instrument itself, even a well-tuned instrument will still be affected by the fragmentation, though to a lesser extent. Notably, a series of water-containing nitrate clusters appear in the spectrum partly due to the soft-tuning. However, as the sum of the water-containing nitrate anions is less than 4% of the sum of nitrate anions in our instrument, water-containing nitrate anions only affect the species with significant abundance, e.g., HIO_3. For measured neutral clusters which normally have a few counts or less than one count per second, the water-containing nitrate anions are unlikely to interfere with the detection.

One of the main results concerning the neutral cluster is that we have directly measured the $2HIO_3 \cdot NO_3^-$ anion in the spectrum for the first time. This is the direct evidence that a neutral HIO_3 dimer can be formed in the atmosphere without being completely converted to I_2O_5, which was

hypothesized by Sipilä *et al*. (*11*). The result also indicates that the conversion of $HIO_3 \cdot HIO_3$ to I_2O_5 does not happen instantaneously even in the presence of negative charge – at least in our soft-tuned instrument; a finite reaction rate may be expected. Additionally, the direct evaporation of HIO_3 from iodine particles (Fig. 5) suggests that bulk HIO_3 can indeed exist in iodine particles. However, we have not so far measured significant amount of HIO_2 in particle phase, indicating either a negligible presence or that it might have been converted to, for example, I_2O_4.

References and notes:

39. J. Duplissy, J. Merikanto, A. Franchin, G. Tsagkogeorgas, J. Kangasluoma, D. Wimmer, H. Vuollekoski, S. Schobesberger, K. Lehtipalo, R. C. Flagan, D. Brus, N. M. Donahue, H. Vehkamäki, J. Almeida, A. Amorim, P. Barmet, F. Bianchi, M. Breitenlechner, E. M. Dunne, R. Guida, H. Henschel, H. Junninen, J. Kirkby, A. Kürten, A. Kupc, A. Määttänen, V. Makhmutov, S. Mathot, T. Nieminen, A. Onnela, A. P. Praplan, F. Riccobono, L. Rondo, G. Steiner, A. Tome, H. Walther, U. Baltensperger, K. S. Carslaw, J. Dommen, A. Hansel, T. Petäjä, M. Sipilä, F. Stratmann, A. Vrtala, P. E. Wagner, D. R. Worsnop, J. Curtius, M. Kulmala, Effect of ions on sulfuric acid-water binary particle formation: 2. Experimental data and comparison with QC-normalized classical nucleation theory. *Journal of Geophysical Research*. **121**, 1752–1775 (2016).

40. F. D. Lopez-Hilfiker, C. Mohr, M. Ehn, F. Rubach, E. Kleist, J. Wildt, T. F. Mentel, A. Lutz, M. Hallquist, D. Worsnop, J. A. Thornton, A novel method for online analysis of gas and particle composition: description and evaluation of a Filter Inlet for Gases and AEROsols (FIGAERO). *Atmospheric Measurement Techniques*. **7**, 983–1001 (2014).

41. H. Junninen, M. Ehn, Petäjä, L. Luosujärvi, T. Kotiaho, R. Kostiainen, U. Rohner, M. Gonin, K. Fuhrer, M. Kulmala, D. R. Worsnop, A high-resolution mass spectrometer to measure atmospheric ion composition. *Atmospheric Measurement Techniques*. **3**, 1039–1053 (2010).

42. T. Jokinen, M. Sipilä, H. Junninen, M. Ehn, G. Lönn, J. Hakala, T. Petäjä, R. L. Mauldin, M. Kulmala, D. R. Worsnop, Atmospheric sulphuric acid and neutral cluster measurements using CI-APi-TOF. *Atmospheric Chemistry and Physics*. **12**, 4117–4125 (2012).

43. A. Kürten, T. Jokinen, M. Simon, M. Sipilä, N. Sarnela, H. Junninen, A. Adamov, J. Almeida, A. Amorim, F. Bianchi, M. Breitenlechner, J. Dommen, N. M. Donahue, J. Duplissy, S. Ehrhart, R. C. Flagan, A. Franchin, J. Hakala, A. Hansel, M. Heinritzi, M. Hutterli, J. Kangasluoma, J. Kirkby, A. Laaksonen, K. Lehtipalo, M. Leiminger, V. Makhmutov, S. Mathot, A. Onnela, T. Petäjä, A. P. Praplan, F. Riccobono, M. P. Rissanen, L. Rondo, S. Schobesberger, J. H. Seinfeld, G. Steiner, A. Tomé, J. Tröstl, P. M. Winkler, C. Williamson, D. Wimmer, P. Ye, U. Baltensperger, K. S. Carslaw, M. Kulmala, D. R. Worsnop, J. Curtius, Neutral molecular cluster formation of sulfuric acid–dimethylamine observed in real time under atmospheric conditions. *Proceedings of the National Academy of Sciences*. **111**, 15019–15024 (2014).

44. R. A. Washenfelder, A. O. Langford, H. Fuchs, S. S. Brown, Measurement of glyoxal using an incoherent broadband cavity enhanced absorption spectrometer. *Atmospheric Chemistry and Physics*. **8**, 7779-7793 (2008).

45. R. Thalman, R. Volkamer, Temperature dependent absorption cross-sections of O_2–O_2 collision pairs between 340 and 630 nm and at atmospherically relevant pressure. *Physical Chemistry Chemical Physics*. **15**, 15371 (2013).

46. J. Vanhanen, J. Mikkilä, K. Lehtipalo, M. Sipilä, H. E. Manninen, E. Siivola, T. Petäjä, M. Kulmala, Particle Size Magnifier for Nano-CN Detection. *Aerosol Science and Technology*. **45**, 533–542 (2011).

47. H. E. Manninen, S. Mirme, A. Mirme, T. Petäjä, M. Kulmala, How to reliably detect molecular clusters and nucleation mode particles withNeutral cluster and Air Ion Spectrometer (NAIS). *Atmospheric Measurement Techniques*. **9**, 3577–3605 (2016).

48. D. Stolzenburg, G. Steiner, P. M. Winkler, A DMA-train for precision measurement of sub-10 nm aerosol dynamics. *Atmospheric Measurement Techniques*. **10**, 1639–1651 (2017).

49. J. Tröstl, T. Tritscher, O. F. Bischof, H.-G. Horn, T. Krinke, U. Baltensperger, M. Gysel, Fast and precise measurement in the sub-20nm size range using a Scanning Mobility Particle Sizer. *Journal of Aerosol Science*. **87**, 75–87 (2015).

50. L. Dada, K. Lehtipalo, J. Kontkanen, T. Nieminen, R. Baalbaki, L. Ahonen, J. Duplissy, C. Yan, B. Chu, T. Petäjä, K. Lehtinen, V.-M. Kerminen, M. Kulmala, J. Kangasluoma, Formation and growth of sub-3-nm aerosol particles in experimental chambers. *Nature Protocols*. **15**, 1013–1040 (2020).

51. K. Lehtipalo, J. Leppa, J. Kontkanen, J. Kangasluoma, A. Franchin, D. Wimnner, S. Schobesberger, H. Junninen, T. Petaja, M. Sipila, Methods for determining particle size distribution and growth rates between 1 and 3 nm using the Particle Size Magnifier. *Boreal Environment Research* (2014).

52. M. J. Frisch, G. W. Trucks, H. B. Schlegel, G. E. Scuseria, M. A. Robb, J. R. Cheeseman, G. Scalmani, V. Barone, B. Mennucci, G. A. Petersson, H. Nakatsuji, M. Caricato, X. Li, H. P. Hratchian, A. F. Izmaylov, J. Bloino, G. Zheng, J. L. Sonnenberg, M. Hada, M. Ehara, K. Toyota, R. Fukuda, J. Hasegawa, M. Ishida, T. Nakajima, Y. Honda, O. Kitao, H. Nakai, T. Vreven, J. A. Montgomery, J. E. Peralta, F. Ogliaro, M. Bearpark, J. J. Heyd, E. Brothers, K. N. Kudin, V. N. Staroverov, R. Kobayashi, J. Normand, K. Raghavachari, A. Rendell, J. C. Burant, S. S. Iyengar, J. Tomasi, M. Cossi, N. Rega, J. M. Millam, M. Klene, J. E. Knox, J. B. Cross, V. Bakken, C. Adamo, J. Jaramillo, R. Gomperts, R. E. Stratmann, O. Yazyev, A. J. Austin, R. Cammi, C. Pomelli, J. W. Ochterski, R. L. Martin, K. Morokuma, V. G. Zakrzewski, G. A. Voth, P. Salvador, J. J. Dannenberg, S. Dapprich, A. D. Daniels, Ö. Farkas, J. B. Foresman, J. V. Ortiz, J. Cioslowski, D. J. Fox, *Gaussian 09, Revision D.01* (Gaussian, Inc., Wallingford CT, 2009).s

53. J. Zhang, M. Dolg, ABCluster: the artificial bee colony algorithm for cluster global optimization. *Physical Chemistry Chemical Physics*. **17**, 24173–24181 (2015).

54. J. Zhang, M. Dolg, Global optimization of clusters of rigid molecules using the artificial bee colony algorithm. *Physical Chemistry Chemical Physics*. **18**, 3003–3010 (2016).

55. K. Vanommeslaeghe, E. Hatcher, C. Acharya, S. Kundu, S. Zhong, J. Shim, E. Darian, O. Guvench, P. Lopes, I. Vorobyov, A. D. Mackerell, *Journal of Computational Chemistry*. **31***, 671-690* (2009).

56. N. Hyttinen, R. V. Otkjær, S. Iyer, H. G. Kjaergaard, M. P. Rissanen, P. O. Wennberg, T. Kurtén, Computational Comparison of Different Reagent Ions in the Chemical Ionization of Oxidized Multifunctional Compounds. *Journal of Physical Chemistry A*. **122**, 269–279 (2018).

57. D. Feller, The role of databases in support of computational chemistry calculations. *Journal of Computational Chemistry*. **17**, 1571–1586 (1996).

58. R. A. Kendall, T. H. Dunning, R. J. Harrison, Electron affinities of the first - row atoms revisited. Systematic basis sets and wave functions. *The Journal of Chemical Physics*. **96**, 6796–6806 (1992).

59. C. Riplinger, F. Neese, An efficient and near linear scaling pair natural orbital based local coupled cluster method. *The Journal of Chemical Physics*. **138**, 034106 (2013).

60. F. Neese, The ORCA program system: The ORCA program system. *Wiley Interdisciplinary Reviews: Computational Molecular Science*. **2**, 73–78 (2012).

61. A. Kürten, C. Li, F. Bianchi, J. Curtius, A. Dias, N. M. Donahue, J. Duplissy, R. C. Flagan, J. Hakala, T. Jokinen, J. Kirkby, M. Kulmala, A. Laaksonen, K. Lehtipalo, V. Makhmutov, A. Onnela, M. P. Rissanen, M. Simon, M. Sipilä, Y. Stozhkov, J. Tröstl, P. Ye, P. H. McMurry, New particle formation in the sulfuric acid–dimethylamine–water system: reevaluation of CLOUD chamber measurements and comparison to an aerosol nucleation and growth model. *Atmospheric Chemistry and Physics*. **18**, 845–863 (2018).

62. A. Kürten, New particle formation from sulfuric acid and ammonia: nucleation and growth model based on thermodynamics derived from CLOUD measurements for a wide range of conditions. *Atmospheric Chemistry and Physics*. **19**, 5033–5050 (2019).

63. S. Khanniche, F. Louis, L. Cantrel, I. Černušák, A theoretical study of the microhydration of iodic acid ($HOIO_2$). *Computational and Theoretical Chemistry*. **1094**, 98–107 (2016).

64. P. Hari, E. Nikinmaa, T. Pohja, E. Siivola, J. Bäck, T. Vesala, M. Kulmala, Station for measuring ecosystem-atmosphere relations: SMEAR. *Physical and Physiological Forest Ecology*. **9789400756**, 471–487 (2013).

65. Y. Zhou, L. Dada, Y. Liu, Y. Fu, J. Kangasluoma, T. Chan, C. Yan, B. Chu, K. R. Daellenbach, F. Bianchi, T. Kokkonen, Y. Liu, J. Kujansuu, V.-M. Kerminen, T. Petäjä, L. Wang, J. Jiang, M. Kulmala, Variation of size-segregated particle number concentrations in winter Beijing. *Atmospheric Chemistry and Physics* **20**, 1201-1216 (2020).

66. C. Deng, Y. Fu, L. Dada, C. Yan, R. Cai, D. Yang, Y. Zhou, R. Yin, Y. Lu, X. Li, X. Qiao, X. Fan, W. Nie, J. Kontkanen, J. Kangasluoma, B. Chu, A. Ding, V.-M. Kerminen, P. Paasonen, D. R. Worsnop, F. Bianchi, Y. Liu, J. Zheng, L. Wang, M. Kulmala, J. Jiang, Seasonal Characteristics of New Particle Formation and Growth in Urban Beijing. *Environ. Sci. Technol.* **54**, 8547–8557 (2020).

67. T. Hussein, J. Martikainen, H. Junninen, L. Sogacheva, R. Wagner, M. D. Maso, I. Riipinen, P. P. Aalto, M. Kulmala, Observation of regional new particle formation in the urban atmosphere. *Tellus B: Chemical and Physical Meteorology*. **60**, 509–521 (2008).

68. S. Wang, J. A. Schmidt, S. Baidar, S. Coburn, B. Dix, T. K. Koenig, E. Apel, D. Bowdalo, T. L. Campos, E. Eloranta, M. J. Evans, J. P. DiGangi, M. A. Zondlo, R.-S. Gao, J. A. Haggerty, S. R. Hall, R. S. Hornbrook, D. Jacob, B. Morley, B. Pierce, M. Reeves, P. Romashkin, A. Ter Schure, R. Volkamer, Active and widespread halogen chemistry in the tropical and subtropical free troposphere. *Proceedings of the National Academy of Sciences*. **112**, 9281–6 (2015).

69. A. Saiz‐Lopez, S. Baidar, C. A. Cuevas, T. K. Koenig, R. P. Fernandez, B. Dix, D. E. Kinnison, J.‐F. Lamarque, X. Rodriguez‐Lloveras, T. L. Campos, R. Volkamer, Injection of iodine to the stratosphere. *Geophysical Research Letters*. **42**, 6852–6859 (2015).

70. I. Pundt, J.-P. Pommereau, C. Phillips, E. Lateltin, Upper Limit of Iodine Oxide in the Lower Stratosphere. *Journal of Atmospheric Chemistry*. **30**, 173–185 (1998).

71. H. Bösch, Upper limits of stratospheric IO and OIO inferred from center-to-limb-darkening-corrected balloon-borne solar occultation visible spectra: Implications for total gaseous iodine and stratospheric ozone. *Journal of Geophysical Research* **108**, 4455 (2003).

72. Yu. I. Stozhkov, N. S. Svirzhevsky, G. A. Bazilevskaya, A. N. Kvashnin, V. S. Makhmutov, A. K. Svirzhevskaya, Long-term (50 years) measurements of cosmic ray fluxes in the atmosphere. *Advances in Space Research*. **44**, 1124–1137 (2009).

73. C. J. Williamson, A. Kupc, D. Axisa, K. R. Bilsback, T. Bui, P. Campuzano-Jost, M. Dollner, K. D. Froyd, A. L. Hodshire, J. L. Jimenez, J. K. Kodros, G. Luo, D. M. Murphy, B. A. Nault, E. A. Ray, B. Weinzierl, J. C. Wilson, F. Yu, P. Yu, J. R. Pierce, C. A. Brock, A large source of cloud condensation nuclei from new particle formation in the tropics. *Nature*. **574**, 399–403 (2019).

74. D. L. Hartmann, L. A. Moy, Q. Fu, Tropical Convection and the Energy Balance at the Top of the Atmosphere. *Journal of Climate*. **14**, 17 (2001).

75. A. Gettelman, Radiation balance of the tropical tropopause layer. *Journal of Geophysical Research*. **109**, D07103 (2004).

76. M. Legrand, J. R. McConnell, S. Preunkert, M. Arienzo, N. Chellman, K. Gleason, T. Sherwen, M. J. Evans, L. J. Carpenter, Alpine ice evidence of a three-fold increase in atmospheric iodine deposition since 1950 in Europe due to increasing oceanic emissions. *Proceedings of the National Academy of Sciences*. **115**, 12136–12141 (2018).

77. X. Zhao, X. Hou, W. Zhou, Atmospheric Iodine (^{127}I and ^{129}I) Record in Spruce Tree Rings in the Northeast Qinghai-Tibet Plateau. *Environmental Science and Technology*. **15**, 8706-8714 (2019)

78. S. Khanniche, F. Louis, L. Cantrel, I. Černušák, Computational study of the $I_2O_5+H_2O=2HOIO_2$ gas-phase reaction. *Chemical Physics Letters*. **662**, 114–119 (2016).

79. M. Passananti, E. Zapadinsky, T. Zanca, J. Kangasluoma, N. Myllys, M. P. Rissanen, T. Kurtén, M. Ehn, M. Attoui, H. Vehkamäki, How well can we predict cluster fragmentation inside a mass spectrometer? *Chemical Communications* **55**, 5946–5949 (2019).

80. R. J. Huang, K. Seitz, J. Buxmann, D. Pöhler, K. E. Hornsby, L. J. Carpenter, U. Platt, T. Hoffmann, In situ measurements of molecular iodine in the marine boundary layer: The link to macroalgae and the implications for O_3, IO, OIO and NO_x. *Atmospheric Chemistry and Physics*. **10**, 4823–4833 (2010).

81. A. Saiz-Lopez, R. W. Saunders, D. M. Joseph, S. H. Ashworth, J. M. C. Plane, Absolute absorption cross-section and photolysis rate of I_2. *Atmospheric Chemistry and Physics*. **4**, 1443–1450 (2004).

Table S1. Comparison of CLOUD experiments with ambient conditions. A summary of ambient measurements of iodine species can be found in Huang *et al.* (*80*). The pI is the iodine atom production rate, which is calculated either from I_2 photolysis or its reaction with NO_3 radicals. In the former case, the photolysis rate is assumed to be at mid-day sun condition, thus representing an upper limit. The I_2 photolysis rate at CLOUD is estimated from I_2 decay experiments at various light settings. We note that the iodine atom production rates from CLOUD and from ambient are not directly comparable as other halogen species and NO_x can consume the produced iodine atoms and other initial iodine oxides in the ambient. This results in a higher yield of iodine oxoacids from iodine atoms in CLOUD than in the ambient. Nevertheless, the I_2, HIO_x and IO concentrations in the CLOUD experiments are comparable to those in the ambient.

Location	I_2 (pptv)	pI ($\times 10^6$ atom cm^{-3} s^{-1})	IO (pptv)
Mace Head day, low tide	20+	[a]100+	4-10+
Mace Head day, high tide	5	[a]30	2-7
Mace Head night (I_2 + NO_3)	few 10	[b]0.5	0.5-4
Open ocean	1	[a]6	0.5-1
CLOUD median	6.4	[c]0.2	[d]1.2
CLOUD min-max	0.4 - 168	[c]0.04-15	[d]0.5-9.6

[a] Estimated from the I_2 concentration and an I_2 photolysis rate of 0.12 s^{-1} with the mid-day sun (*81*).
[b] Estimated from the 10 pptv I_2, 50 pptv NO_3 and a reaction rate coefficient of 1.5×10^{-12} cm^3 s^{-1} with NO_3.
[c] Estimated from I_2 concentrations and light fluxes of the reported experiments. The systematic uncertainty is a factor three.
[d] A systematic uncertainty of a factor of three is estimated for these measurements.

Table S2. Molecular composition of charged and neutral clusters shown in Fig. 2. The charged clusters (Fig. 2A) are produced by gcr ions in the CLOUD chamber. The neutral clusters (Figs. 2B and S4) are charged in the nitrate-CIMS by NO_3^- or $HNO_3 \cdot NO_3^-$ ions, as indicated in the table. Some of the clusters are ambiguous since we could not resolve whether I_2O_4 or I_2O_5 is present. In order to simplify Fig. 2B, all clusters with the same iodine molecular composition are summed into a single point, i.e., they are summed over all water molecules and nitrate charger ions.

Charged clusters (Fig. 2A) (charged by gcr ions)	**No. iodine atoms**	**Mass/charge, *m/z* (Th)**	**Signal (cps)**
Pure HIO_3 / HIO_2 clusters (orange)			
IO_2^-	1	158.895	0.331
$HIO_2 \cdot IO_3^-$	2	334.791	0.021
$HIO_3 \cdot HIO_2 \cdot IO_3^-$	3	510.689	0.502
HIO_3 / I_2O_5 clusters (blue)			
IO_3^-	1	174.890	40.423
$H_2O \cdot IO_3^-$	1	192.900	1.341
$HIO_3 \cdot NO_3^-$	1	237.885	10.386
$HIO_3 \cdot IO_3^-$	2	350.787	8.468
$I_2O_5 \cdot IO_3^-$	3	508.673	5.259
$HIO_3 \cdot I_2O_5 \cdot IO_3^-$	4	684.570	2.946
$2I_2O_5 \cdot IO_3^-$	5	842.457	2.062
Mixed HIO_3 / HIO_2 clusters (pink)			
$I_2O_4 \cdot IO_3^-$	3	492.678	0.250
$HIO_3 \cdot I_2O_5 \cdot IO_3^-$	4	668.575	0.347
$I_2O_5 \cdot I_2O_4 \cdot IO_3^-$	5	826.461	0.430
Neutral clusters (Figs. 2B and S4) (charged by nitrate anions)	**No. iodine atoms**	**Mass/charge, *m/z* (Th)**	**Signal (cps)**
Pure HIO_3 / HIO_2 clusters (orange)			
$HIO_2 \cdot NO_3^-$	1	221.885	1.638
$HIO_2 \cdot HNO_3NO_3^-$	1	284.885	38.347
$HIO_3 \cdot HIO_2 \cdot NO_3^-$	2	397.788	79.746
$HIO_3 \cdot HIO_2 \cdot H_2O \cdot NO_3^-$	2	415.798	0.708
$HIO_3 \cdot HIO_2 \cdot 2H_2O \cdot NO_3^-$	2	433.810	0.795
$HIO_3 \cdot HIO_2 \cdot 3H_2O \cdot NO_3^-$	2	451.820	0.632
$HIO_3 \cdot HIO_2 \cdot HNO_3NO_3^-$	2	460.784	10.120
$HIO_3 \cdot HIO_2 \cdot 4H_2O \cdot NO_3^-$	2	469.831	0.564
$HIO_3 \cdot HIO_2 \cdot H_2O \cdot HNO_3NO_3^-$	2	478.794	0.299
$HIO_3 \cdot HIO_2 \cdot 5H_2O \cdot NO_3^-$	2	487.843	0.408
$HIO_3 \cdot HIO_2 \cdot 2H_2O \cdot HNO_3NO_3^-$	2	496.808	0.380
$HIO_3 \cdot HIO_2 \cdot 6H_2O \cdot NO_3^-$	2	505.853	0.289
$HIO_3 \cdot HIO_2 \cdot 3H_2O \cdot HNO_3NO_3^-$	2	514.816	0.346
$HIO_3 \cdot HIO_2 \cdot 7H_2O \cdot NO_3^-$	2	523.865	0.254
$HIO_3 \cdot HIO_2 \cdot IO_3^-$	3	510.691	0.344
$2HIO_3 \cdot HIO_2 \cdot NO_3^-$	3	573.688	0.455
$2HIO_3 \cdot 2HIO_2 \cdot NO_3^-$	4	733.592	0.517
$2HIO_3 \cdot 2HIO_2 \cdot IO_3^-$	5	846.491	1.560
$3HIO_3 \cdot 2HIO_2 \cdot NO_3^-$	5	909.488	0.306

HIO_3 / I_2O_5 clusters (blue)			
IO_3^-	1	174.889	194.174
$HIO_3 \cdot NO_3^-$	1	237.884	2472.274
$HIO_3 \cdot H_2O \cdot NO_3^-$	1	255.895	23.859
$HIO_3 \cdot 2H_2O \cdot NO_3^-$	1	273.906	11.635
$HIO_3 \cdot 3H_2O \cdot NO_3^-$	1	291.916	12.686
$HIO_3 \cdot HNO_3NO_3^-$	1	300.880	782.010
$HIO_3 \cdot 4H_2O \cdot NO_3^-$	1	309.927	11.424
$HIO_3 \cdot H_2O \cdot HNO_3NO_3^-$	1	318.891	3.730
$HIO_3 \cdot 5H_2O \cdot NO_3^-$	1	327.938	7.137
$HIO_3 \cdot 2H_2O \cdot HNO_3NO_3^-$	1	336.902	4.041
$HIO_3 \cdot 6H_2O \cdot NO_3^-$	1	345.948	6.362
$HIO_3 \cdot 3H_2O \cdot HNO_3NO_3^-$	1	354.913	4.141
$HIO_3 \cdot 7H_2O \cdot NO_3^-$	1	363.959	5.349
$HIO_3 \cdot 4H_2O \cdot HNO_3NO_3^-$	1	372.923	3.276
$HIO_3 \cdot 8H_2O \cdot NO_3^-$	1	381.970	4.057
$HIO_3 \cdot 5H_2O \cdot HNO_3NO_3^-$	1	390.934	3.575
$HIO_3 \cdot 9H_2O \cdot NO_3^-$	1	399.981	3.741
$HIO_3 \cdot 6H_2O \cdot HNO_3NO_3^-$	1	408.945	3.147
$HIO_3 \cdot 10H_2O \cdot NO_3^-$	1	417.992	2.500
$HIO_3 \cdot 7H_2O \cdot HNO_3NO_3^-$	1	426.956	2.027
$HIO_3 \cdot 11H_2O \cdot NO_3^-$	1	436.002	2.437
$HIO_3 \cdot 8H_2O \cdot HNO_3NO_3^-$	1	444.966	1.645
$HIO_3 \cdot 12H_2O \cdot NO_3^-$	1	454.013	2.259
$HIO_3 \cdot 9H_2O \cdot HNO_3NO_3^-$	1	462.978	1.349
$HIO_3 \cdot 13H_2O \cdot NO_3^-$	1	472.024	1.306
$HIO_3 \cdot 10H_2O \cdot HNO_3NO_3^-$	1	480.989	1.101
$HIO_3 \cdot 14H_2O \cdot NO_3^-$	1	490.034	1.172
$HIO_3 \cdot 11H_2O \cdot HNO_3NO_3^-$	1	498.998	0.806
$HIO_3 \cdot 15H_2O \cdot NO_3^-$	1	508.046	0.826
$HIO_3 \cdot 12H_2O \cdot HNO_3NO_3^-$	1	517.011	0.599
$HIO_3 \cdot 16H_2O \cdot NO_3^-$	1	526.057	0.677
$I_2O_5 \cdot NO_3^-$	2	395.773	6.398
$2HIO_3 \cdot NO_3^-$	2	413.784	3.811
$I_2O_5 \cdot IO_3^-$	3	508.675	0.423
Mixed HIO_3 / HIO_2 clusters (pink)			
$I_2O_4 \cdot NO_3^-$	2	379.777	3.654
$I_2O_4 \cdot HNO_3NO_3^-$	2	442.773	34.927
$HIO_3 \cdot I_2O_4 \cdot NO_3^-$	3	555.676	1.887
$2I_2O_4 \cdot NO_3^-$	4	697.565	0.411
$HIO_3 \cdot HIO_2 \cdot I_2O_4 \cdot NO_3^-$	4	715.579	1.583
$2I_2O_4 \cdot IO_3^-$	5	810.470	0.435
$HIO_3 \cdot HIO_2 \cdot I_2O_4 \cdot IO_3^-$	5	828.480	1.985
$HIO_3 \cdot 2I_2O_4 \cdot NO_3^-$	5	873.466	0.339
$2HIO_3 \cdot HIO_2 \cdot I_2O_4 \cdot NO_3^-$	5	891.477	0.297
Other iodine clusters (red)			

$IO \cdot NO_3^-$	1	204.885	0.707
$OIO \cdot NO_3^-$	1	220.881	145.760
$OIO \cdot HNO_3NO_3^-$	1	283.877	84.952
$I_2O_2 \cdot NO_3^-$	2	347.786	4.121
$I_2O_3 \cdot NO_3^-$	2	363.782	6.426

Table S3. Cluster formation free energies for neutral clusters. The quantum chemical calculations are based on (DLPNO-CCSD(T)/def2-QZVPP//ωB97xD/aug-cc-pVTZ-PP level) at 283.15 K and 1 atm. The optimized geometries at the ωB97xD/aug-cc-pVTZ-PP level are shown in fig. S7. The most stable dimer with HIO_3 is $HIO_3 \cdot HIO_2$.

Cluster	Formation free energy (kcal mol^{-1})
$HIO_3 \cdot HIO_3$	-7.7
$HIO_3 \cdot HIO_2$	-12.9
$HIO_2 \cdot HIO_2$	-13.1
$HIO_3 \cdot I_2O_5$	-9.3
$HIO_3 \cdot NH_3$	-5.0
$HIO_3 \cdot HOI$	-1.6

Table S4. Reaction free energies and calculated evaporation rates for charged clusters. The quantum chemical calculations are based on (DLPNO-CCSD(T)/def2-QZVPP//ωB97xD/aug-cc-pVTZ-PP level) at 283.15 K and 1 atm.

Evaporation process	**Reaction Free Energy (kcal mol^{-1})**	**Evaporation rate (s^{-1})**
$I_2O_5 \cdot IO_3^- \rightarrow I_2O_5 + IO_3^-$	31.1	4.2×10^{-14}
$HIO_3 \cdot I_2O_5 \cdot IO_3^- \rightarrow I_2O_5 \cdot HIO_3 + IO_3^-$	43.5	1.1×10^{-23}
$HIO_3 \cdot I_2O_5 \cdot IO_3^- \rightarrow I_2O_5 \cdot IO_3^- + HIO_3$	21.6	9.6×10^{-07}
$HIO_3 \cdot I_2O_5 \cdot IO_3^- \rightarrow HIO_3 \cdot IO_3^- + I_2O_5$	27.1	4.6×10^{-11}
$HIO_3 \cdot IO_3^- \rightarrow HIO_3 + IO_3^-$	25.6	7.2×10^{-10}
$HIO_3 \cdot HIO_3 \cdot IO_3^- \rightarrow HIO_3 \cdot IO_3^- + HIO_3$	17.4	1.6×10^{-03}
$HIO_3 \cdot HIO_3 \cdot IO_3^- \rightarrow HIO_3 \cdot HIO_3 + IO_3^-$	33.6	3.4×10^{-16}

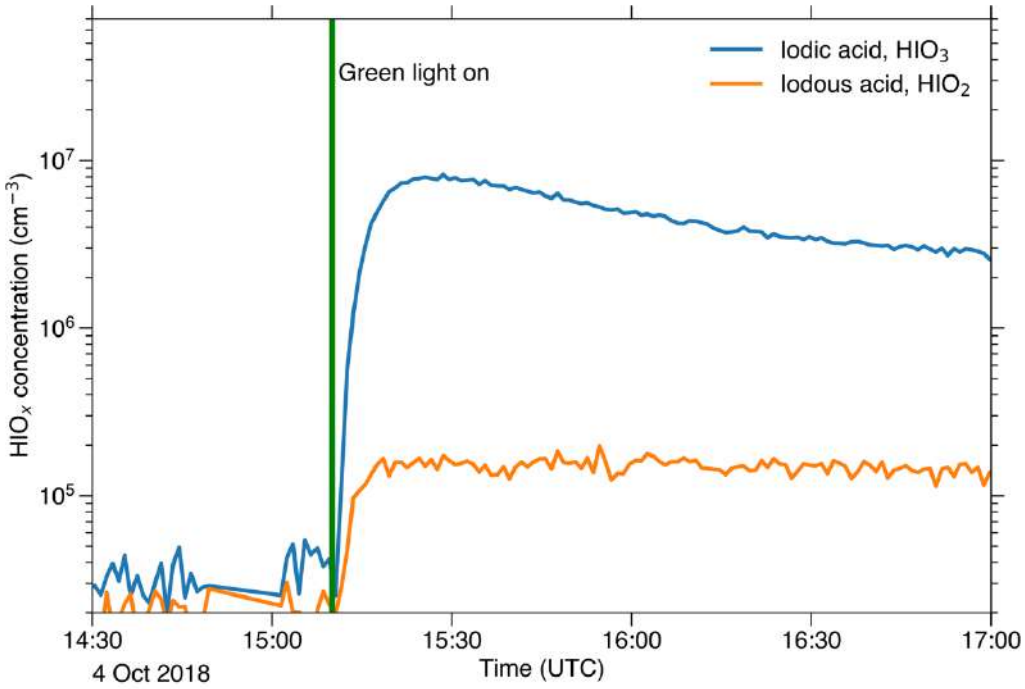

Fig. S1. Formation of iodine oxoacids without HO_x radicals. Gas-phase HIO_3 and iodous acid (HIO_2) measured in the CLOUD chamber before and after switching on green light (528 nm). The experimental conditions are 7 pptv I_2, I atoms production rate of 6.2×10^4 $cm^{-3}s^{-1}$, 40 ppbv ozone, 69% RH and −10°C. Green light photolyzes I_2 to iodine atoms but does not photolyze ozone and so HO_x is absent. This demonstrates that HIO_x can be produced by oxidation with ozone in the absence of HO_x. The measured HIO_2 concentration assumes the same mass-spectrometer calibration factor as for HIO_3, and so represents a lower limit.

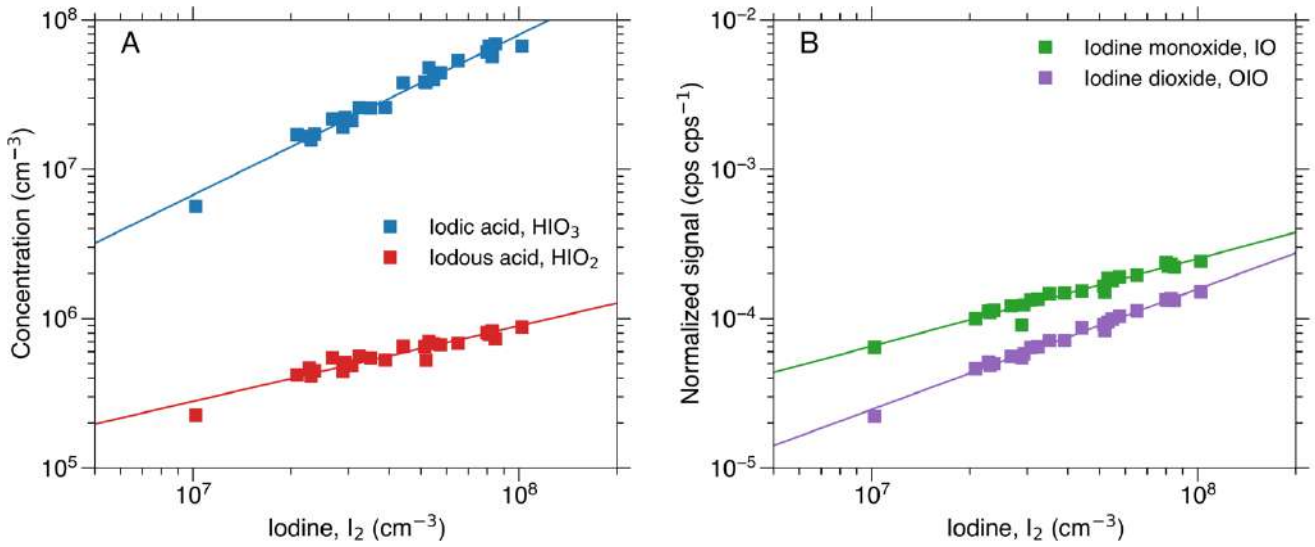

Fig. S2. Iodine oxoacid and oxide production versus I_2. (A) measured concentrations of iodine oxoacids and B) normalized signals of iodine oxides when iodine vapor is adjusted between equilibrium mixing ratios of 0.4 and 4 pptv at fixed experimental conditions of 38 to 42 ppbv O_3, 34 to 44% RH and +10°C. The I atom production rate is 4.4×10^4 cm^{-3} s^{-1} to 3.8×10^5 cm^{-3} s^{-1}. HIO_x is measured with a nitrate-CIMS, and IO, OIO and I_2 are measured with a bromide-CIMS. The lines are power-law fits to the HIO_3 and HIO_2 concentrations of the form $HIO_x = k \times I_2^n$, with fitted values for n of (1.07±0.04) and (0.51±0.04), respectively, and the power-law fits to the IO and OIO normalized signals of the form $IO_x = k \times I_2^n$, with fitted values for n of (0.59±0.03) and (0.81±0.02), respectively.

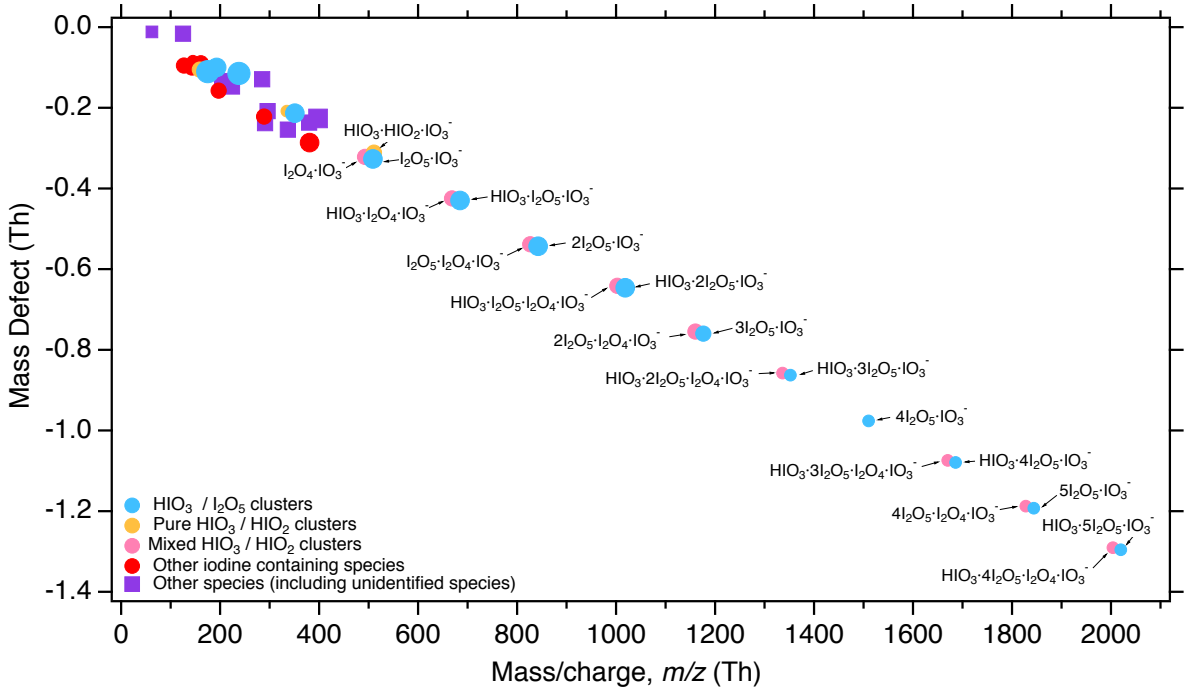

Fig. S3. Ion-induced iodic acid nucleation. Cluster mass defect versus *m/z* of negatively charged clusters containing up to twelve iodine atoms, measured with the APiTOF(−). These data are the same as in Fig. 2A but extended to a higher mass range. The experimental conditions are 36 ppbv O_3, 40% RH, +10°C, 168 pptv I_2 and 1.5×10^7 I atoms cm^{-3} s^{-1}. Blue circles indicate clusters containing only HIO_3 and I_2O_5. Orange circles indicate clusters containing only HIO_3 and HIO_2. Pink circles indicate clusters containing HIO_3, HIO_2, I_2O_5 and I_2O_4. Red circles indicate other iodine-containing neutral clusters. Purple squares indicate species without iodine, of which some are unidentified. The four sizes of symbol, from smallest to largest, indicate the signal strength (counts per second, cps) on a logarithmic scale: 1 (< 0.1 cps), 2 (0.1-1 cps), 3 (1-10 cps) and 4 (>10 cps).

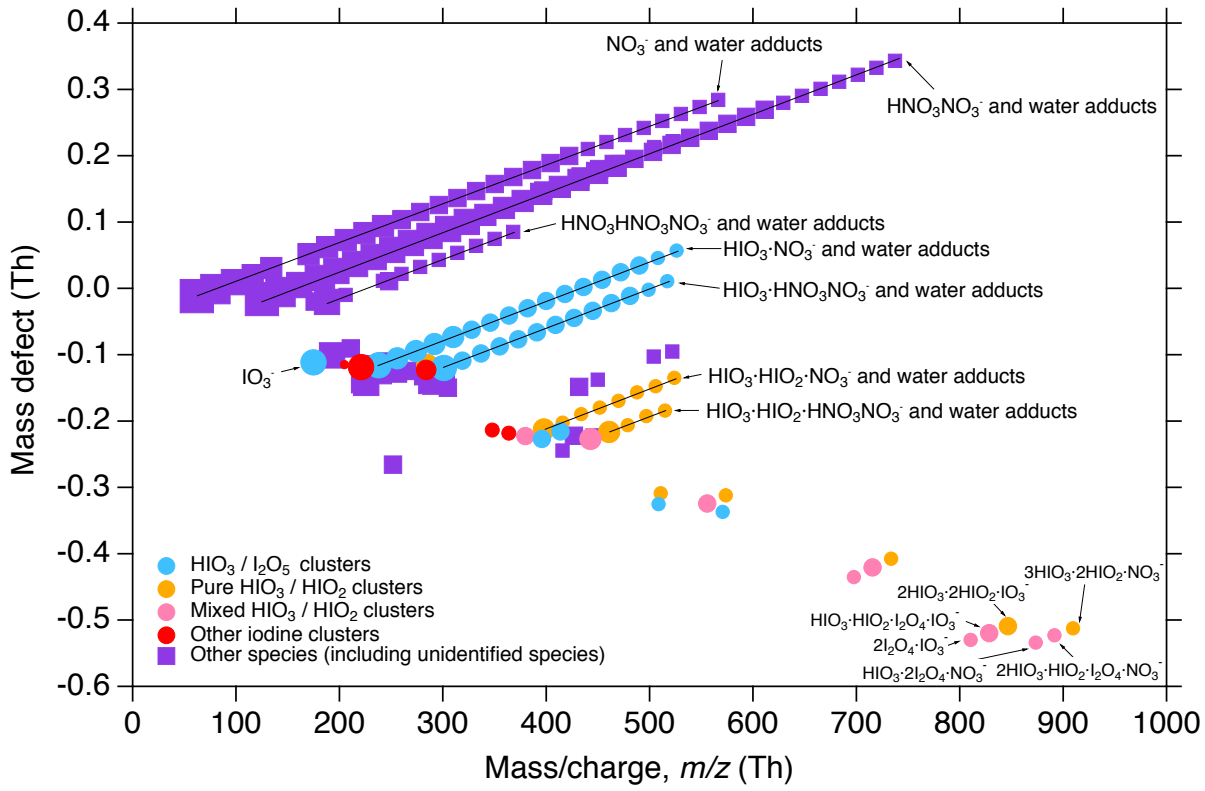

Fig. S4. Neutral nucleation of iodine oxoacids. Cluster mass defect versus *m/z* of neutral clusters containing up to five iodine atoms, measured with the nitrate-CIMS (preceded by an ion filter). These data are the same as in Fig. 2B but showing all identified peaks without summing over water molecules or charger ions. The experimental conditions are 46 ppbv O_3, 43% RH, +10°C, 49 pptv I_2 and 2.4×10^5 I atoms $cm^{-3}s^{-1}$. Blue circles indicate clusters containing only HIO_3 and I_2O_5. Orange circles indicate clusters containing only HIO_3 and HIO_2. Pink circles indicate clusters containing HIO_3, HIO_2, I_2O_5 and I_2O_4. Red circles indicate other iodine-containing clusters. Purple squares indicate species without iodine, of which some are unidentified. The diagonal bands indicate clusters with sequential addition of up to 34 water molecules. The six sizes of symbol, from smallest to largest, indicate the signal strength (counts per second, cps) on a logarithmic scale: 1 (<1 cps), 2 (1-10 cps), 3 (10-100 cps), 4 (100-1000 cps), 4 (1000-10000 cps), and 6 (10000 cps).

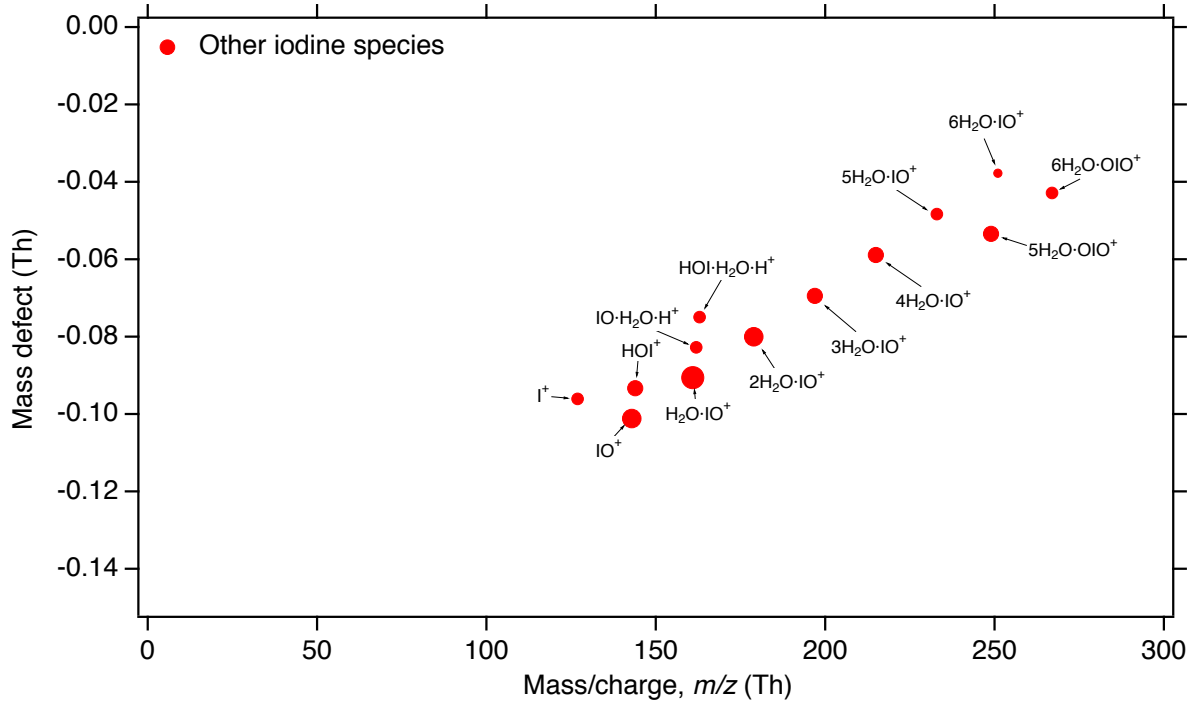

Fig. S5. Positively charged iodine clusters during a nucleation event. Cluster mass defect versus *m/z* of positively charged clusters during a nucleation event, measured with the APiTOF(+). The experimental conditions are 40 ppbv O_3, 34% RH and +10°C, 1.2 pptv I_2 and 1.1×10^5 I atoms $cm^{-3}s^{-1}$. Red circles represent clusters containing one iodine atom. No positively charged clusters were observed containing more than one iodine atom. The four sizes of symbol, from smallest to largest, indicate the signal strength (counts per second, cps) on a logarithmic scale: 1 (< 0.1 cps), 2 (0.1-1 cps), 3 (1-10 cps) and 4 (>10 cps).

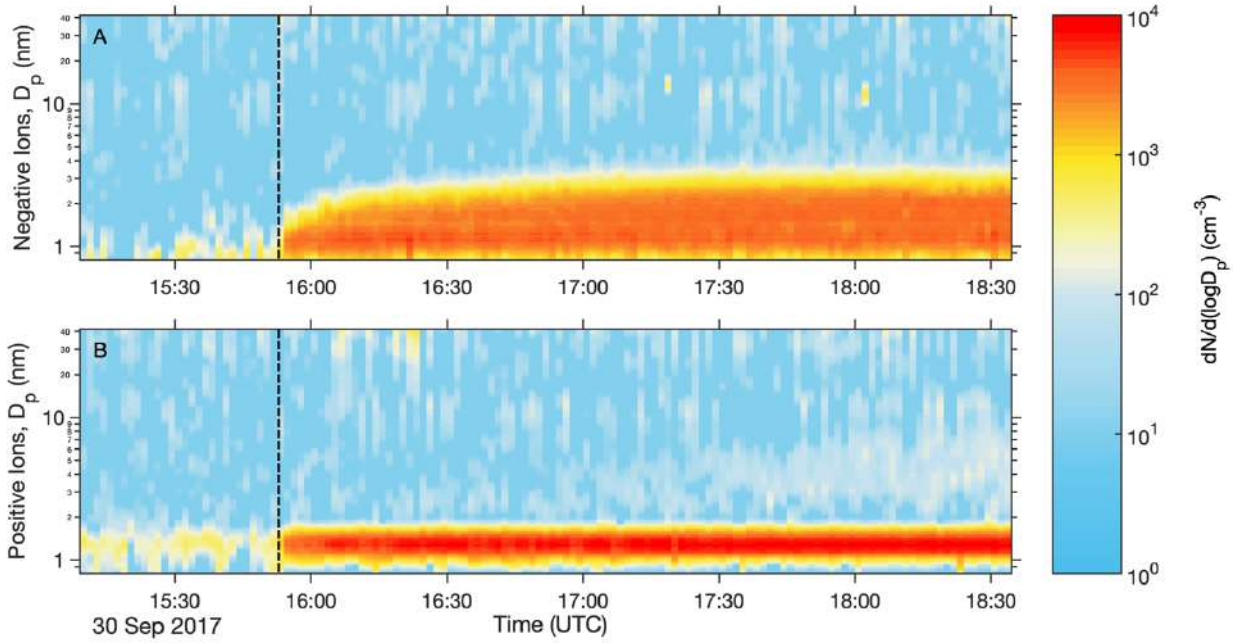

Fig. S6. Evolution of charged particles during a nucleation event. Evolution of the size distribution of (A) negative and (B) positive charged particles measured with the NAIS (Neutral cluster and Air Ion Spectrometer) during a nucleation event. The experimental conditions are 40 ppbv O_3, 34% RH, +10°C, 1.2 pptv I_2 and 1.1×10^5 I atoms cm^{-3} s^{-1}, and zero beam. The vertical dashed line represents the start of the experiment, initiated by turning off the electric field in the chamber and switching on the green light. Small ions of both polarities then build up due to galactic cosmic ray ionization, but nucleation and growth only take place for negative ions. Under these experimental conditions, the negative particles are almost completely neutralized by charge recombination by the time they reach 3 nm, and they continue to grow as mainly neutral particles.

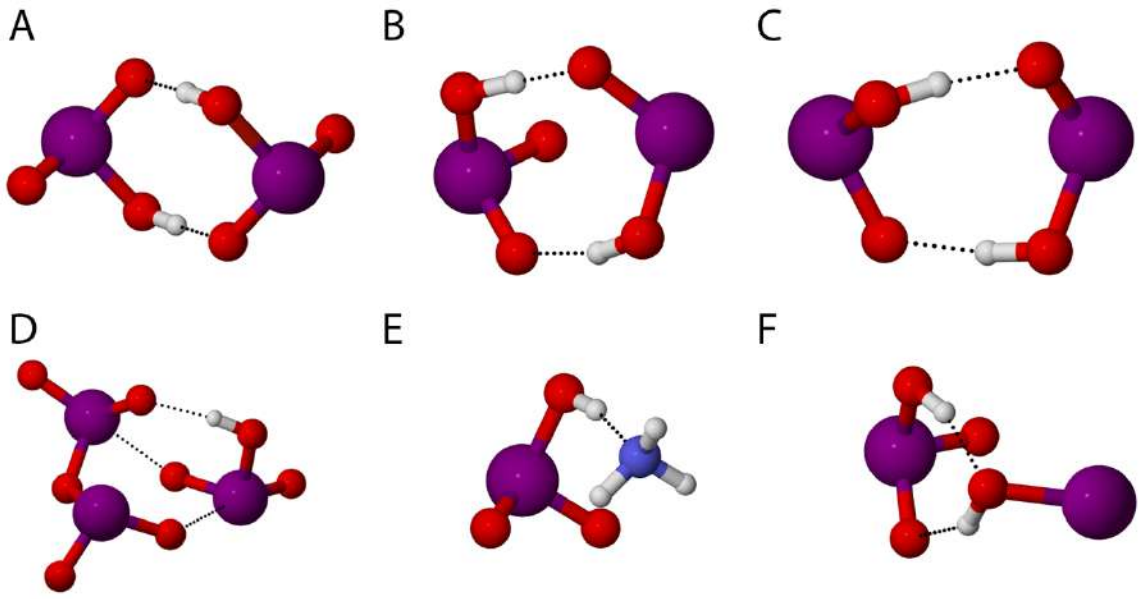

Fig. S7. Lowest free energy neutral dimers containing iodine oxoacids. The lowest free energy cluster geometries for (A) $HIO_3 \cdot HIO_3$, (B) $HIO_3 \cdot HIO_2$, (C) $HIO_2 \cdot HIO_2$, (D) $I_2O_5 \cdot HIO_3$, (E) $HIO_3 \cdot NH_3$, and (F) $HIO_3 \cdot HOI$. The colored balls indicate atoms of iodine (purple), oxygen (red), hydrogen (white), or nitrogen (blue). The clusters are optimized at the ωB97X-D/aug-cc-pVTZ-PP level at 283.15 K. The cluster free energies are summarized in table S3. The most stable dimer with HIO_3 is $HIO_3 \cdot HIO_2$ (dimer B).

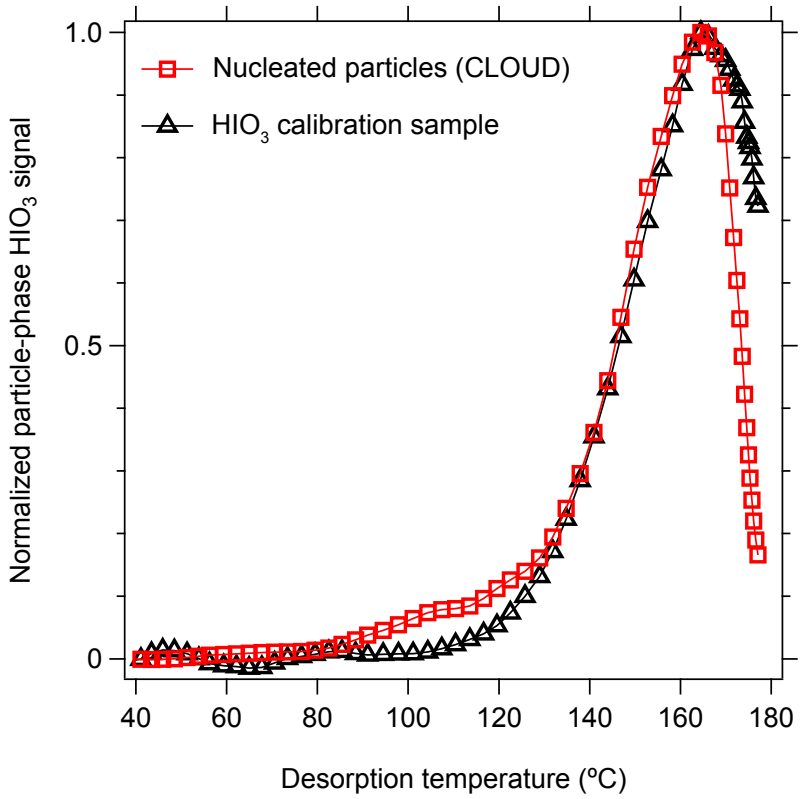

Fig. S8. Comparison of FIGAERO thermograms for iodic acid. Normalized Br^--FIGAERO thermograms of evaporated HIO_3 samples obtained from an iodine oxoacid particle formation experiment in CLOUD (red squares) and from a nebulized pure HIO_3 calibration sample in the laboratory (black triangles). The two thermograms agree well.

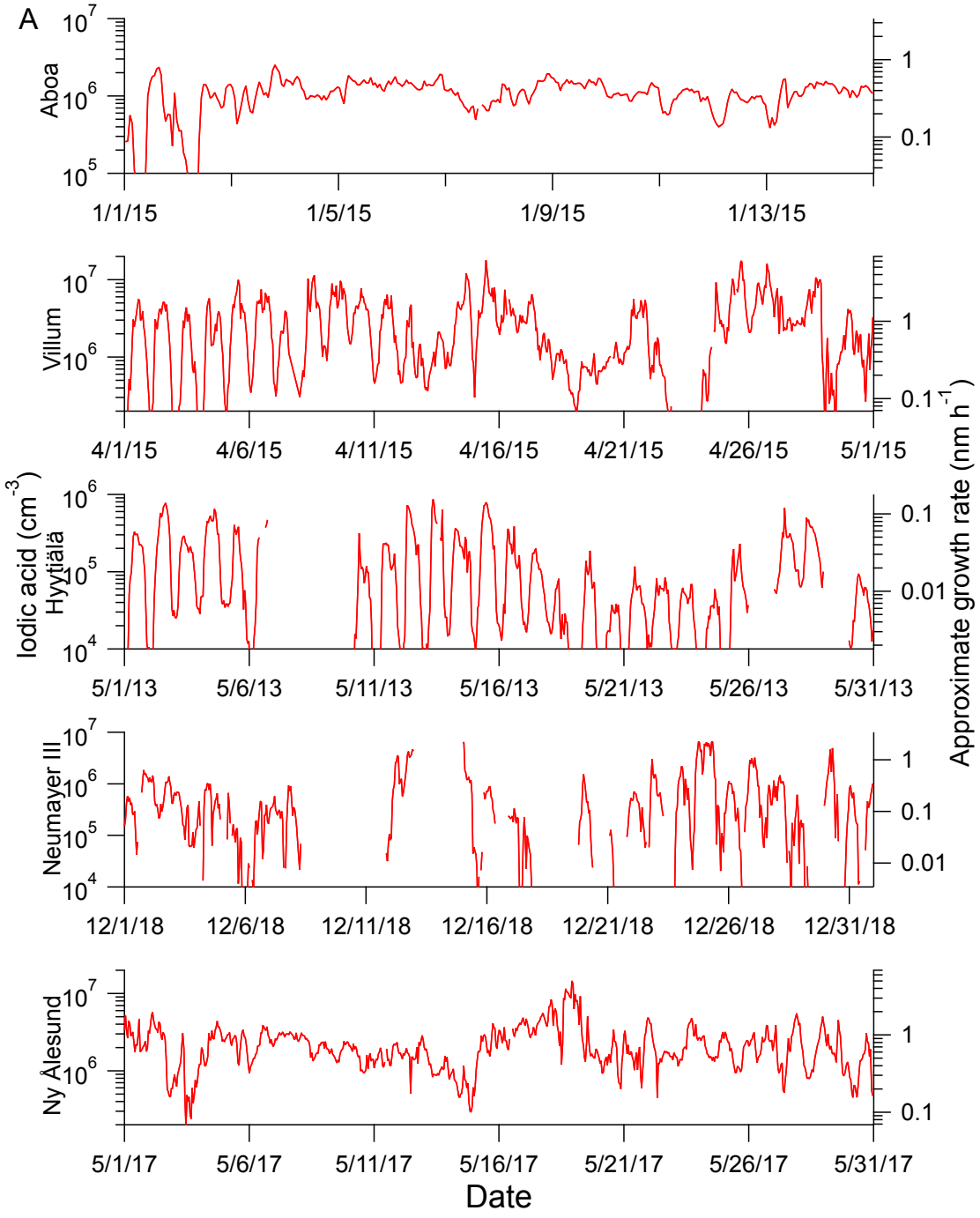
A
Aboa
Villum
Hyytiälä
Neumayer III
Ny Ålesund
Iodic acid (cm-3)
Approximate growth rate (nm h-1)
1/1/15
1/5/15
1/9/15
1/13/15
4/1/15
4/6/15
4/11/15
4/16/15
4/21/15
4/26/15
5/1/15
5/1/13
5/6/13
5/11/13
5/16/13
5/21/13
5/26/13
5/31/13
12/1/18
12/6/18
12/11/18
12/16/18
12/21/18
12/26/18
12/31/18
5/1/17
5/6/17
5/11/17
5/16/17
5/21/17
5/26/17
5/31/17
Date

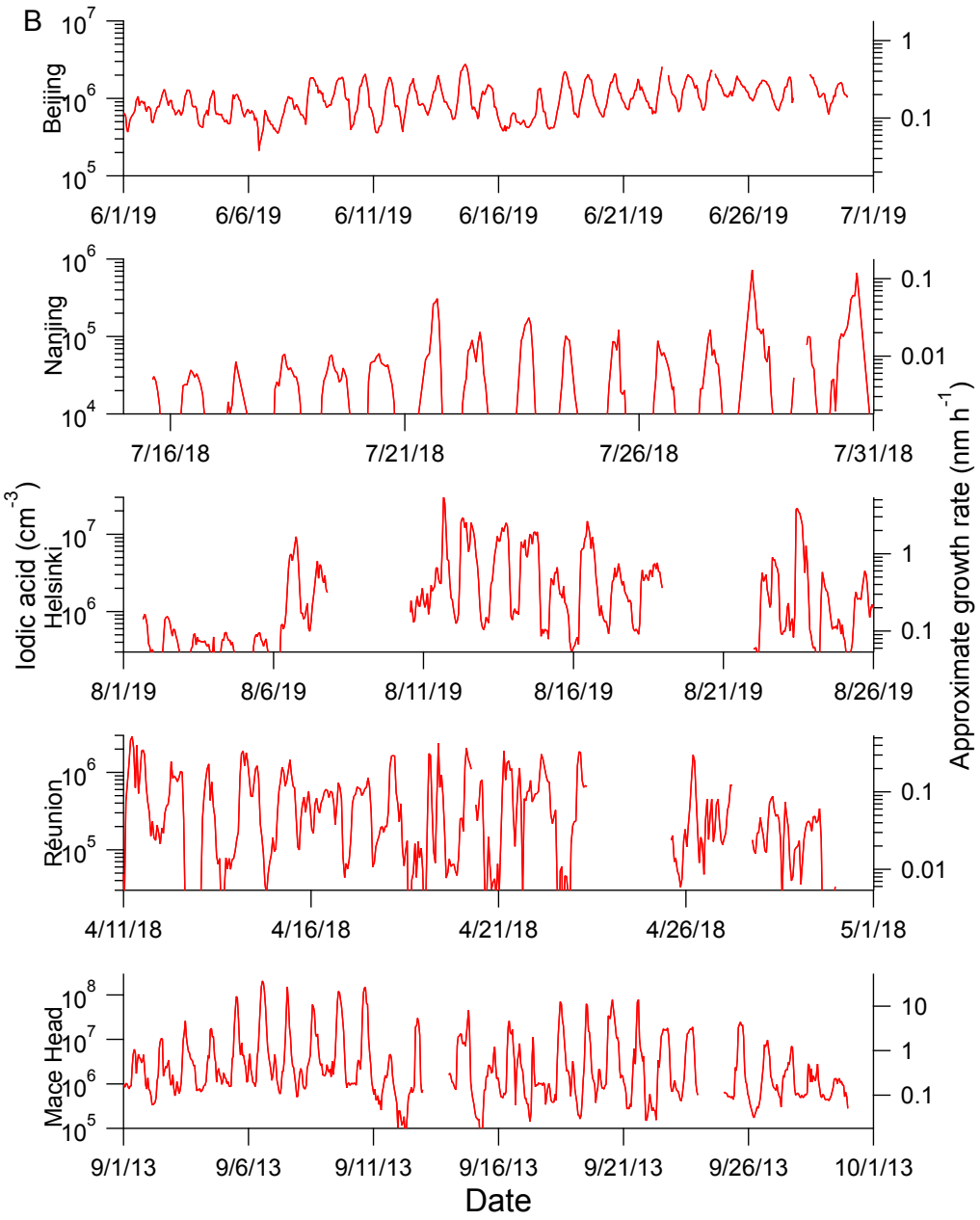

Fig. S9. Iodic acid measurements at diverse sites. HIO_3 concentrations measured at various locations, comprising cities (Beijing and Nanjing, China; Helsinki, Finland), boreal forest (Hyytiälä, Finland), polar regions (Ny Ålesund, Svalbard; Villum research station, Greenland; Aboa and Neumayer III, Antarctica), a coastal marine site (Mace Head, Ireland) and a high altitude site on a tropical island (Réunion, Indian Ocean, at 2160 m). The left axis shows the HIO_3 concentrations, and the right axis shows the approximate expected particle growth rates based on the measurements reported in Fig. 1B. Our growth rates at −10°C are used to estimate those of all the sites with monthly average temperature below 0°C (Ny Ålesund, Villum research station, Aboa and Neumayer III). Growth rates that we measure at +10°C are used for all other sites (Nanjing, Beijing, Helsinki, Hyytiälä, Mace Head and Réunion).

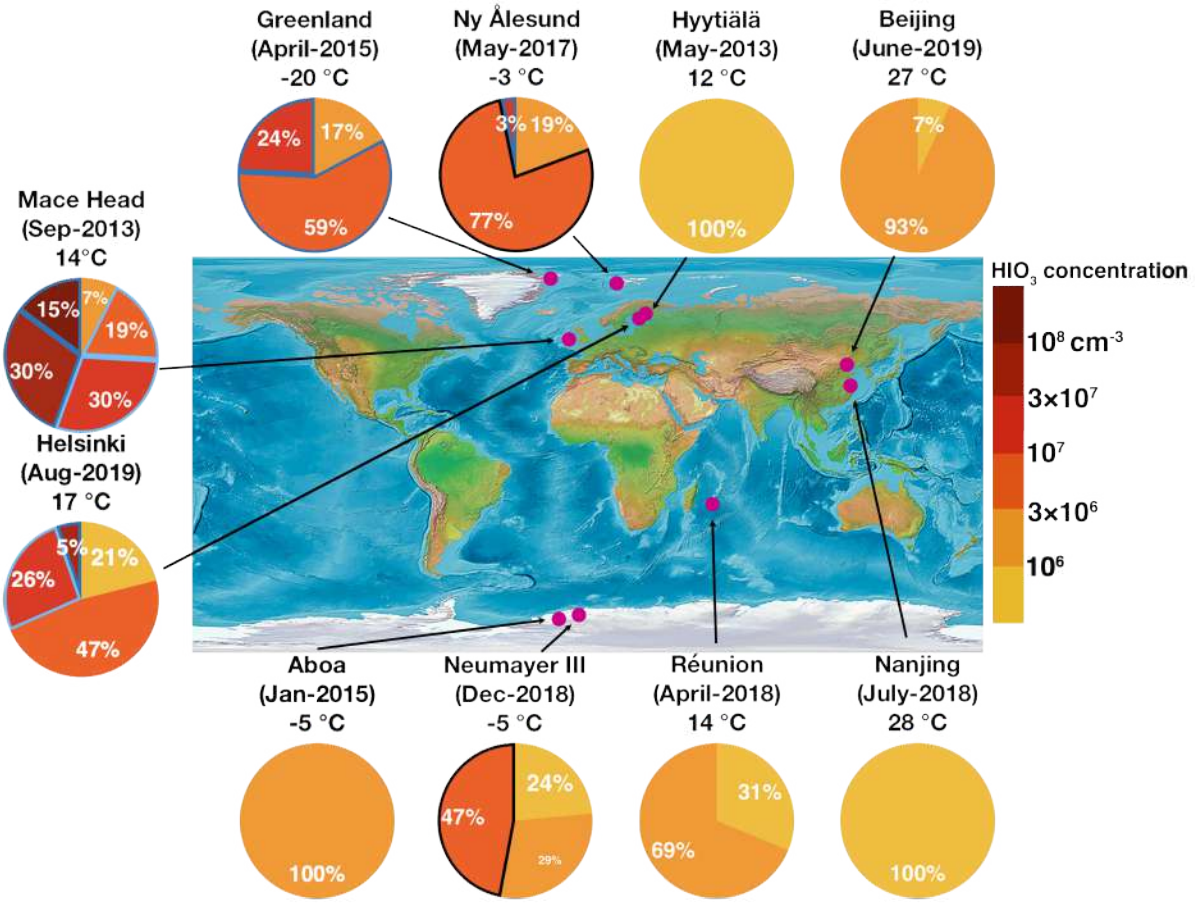

Fig. S10. Frequency of daily maxima of iodic acid at diverse sites. Pie charts showing the percentage of days where the daily HIO_3 maxima fall into the indicated range (evaluated for one-hour-averaged data). Each pie chart represents 2-4 weeks' data at the location, date and mean temperature indicated. Additional information on the sites is provided in section 3. Sectors outlined by light blue and dark blue lines indicate that iodine oxoacid particle formation is expected to be dominated by ion-induced or neutral nucleation, respectively. Sectors outlined by a black line indicate comparable ion-induced and neutral nucleation rates. Sectors without any outline indicate that the expected nucleation rates are below 0.01 cm^{-3} s^{-1}. The systematic uncertainty between HIO_3 measurements at different sites is estimated to be a factor three. All measurements are above the HIO_3 detection limit of the instruments.